

The impact of simulated mesoscale convective systems on global precipitation: A
multi-scale modeling study

Wei-Kuo Tao¹ and Jiun-Dar Chern²

¹*Mesoscale Atmospheric Processes Laboratory
NASA Goddard Space Flight Center
Greenbelt, Maryland*

²*Earth System Science Interdisciplinary Center
University of Maryland
College Park, Maryland*

J. Adv. Model. Earth Syst.

Three key Points:

- *The degree to which MCSs are resolved in multi-scale modeling frameworks (MMFs) can impact their global surface rainfall amount*
- *Surface evaporation and the large-scale wind together determine the tropical rainfall*
- *An MMF with more grid points and finer resolution in its embedded CRMs can produce accurate precipitation statistics*

January 19, 2017

Corresponding author address: Dr. Wei-Kuo Tao, Code 612,
Mesoscale Atmospheric Processes Laboratory, NASA/GSFC, Greenbelt, MD 20771

Abstract

The importance of precipitating mesoscale convective systems (MCSs) has been quantified from TRMM precipitation radar and microwave imager retrievals. MCSs generate more than 50% of the rainfall in most tropical regions. MCSs usually have horizontal scales of a few hundred kilometers (km); therefore, a large domain with several hundred km is required for realistic simulations of MCSs in cloud-resolving models (CRMs). Almost all traditional global and climate models do not have adequate parameterizations to represent MCSs. Typical multi-scale modeling frameworks (MMFs) may also lack the resolution (4 km grid spacing) and domain size (128 km) to realistically simulate MCSs.

In this study, the impact of MCSs on precipitation is examined by conducting model simulations using the Goddard Cumulus Ensemble (GCE) model and Goddard MMF (GMMF). The results indicate that both models can realistically simulate MCSs with more grid points (i.e., 128 and 256) and higher resolutions (1 or 2 km) compared to those simulations with fewer grid points (i.e., 32 and 64) and low resolution (4 km). The modeling results also show the strengths of the Hadley circulations, mean zonal and regional vertical velocities, surface evaporation, and amount of surface rainfall are weaker or reduced in the GMMF when using more CRM grid points and higher CRM resolution. In addition, the results indicate that large-scale surface evaporation and wind feed back are key processes for determining the surface rainfall amount in the GMMF. A sensitivity test with reduced sea surface temperatures shows both reduced surface rainfall and evaporation.

52 **1. Introduction**

53

54 Continued advancements in computational technology now allow general circulation
 55 models (GCMs) to begin to resolve individual convective clouds and convective
 56 systems. Though still computationally very demanding (~ a million times more than a
 57 traditional GCM), global cloud-resolving (or cloud-permitting) models (GCRMs) with
 58 horizontal grid spacing from 3.5 to 14 km have been successfully used in many short-
 59 term atmospheric studies [e.g., *Tomita et al.*, 2005; *Satoh et al.*, 2005, 2008, 2014;
 60 *Putman and Suarez*, 2011; *Miyamoto et al.*, 2013; *Skamarock et al.*, 2014; *Yashiro et*
 61 *al.*, 2016] as well as a long-term (20 years with 14 km resolution) climate simulation
 62 [*Kodama et al.*, 2015]. Another more economical approach to global cloud-resolving
 63 (or cloud-permitting) modeling is the multi-scale modeling framework (MMF) wherein
 64 conventional cloud parameterizations are replaced with a cloud-resolving model
 65 (CRM) in each grid column of a GCM [*Grabowski and Smolarkiewicz*, 1999;
 66 *Khairoutdinov and Randall*, 2001; *Khairoutdinov et al.*, 2005; *Randall et al.*, 2003;
 67 *Tao et al.*, 2009 and papers listed in Table 1]. An MMF can explicitly simulate deep
 68 convection, cloudiness and cloud overlap and cloud-radiation interactions at the
 69 resolution of a CRM. It expands traditional CRM modeling to a global coverage and
 70 enables two-way interactions between the cloud and large scales.

71

72 The first MMF (called SPCAM¹) was developed at Colorado State University (CSU)
 73 [*Khairoutdinov and Randall* 2001; *Randall et al.*, 2003], using the System for

¹ SPCAM stands for superparameterized community atmosphere model.

74 Atmospheric Modeling (SAM, a CRM) to replace the convection parameterizations in
 75 the National Center for Atmospheric Research (NCAR) Community Atmosphere
 76 Model (CAM). It has been used to study a wide variety of atmospheric phenomena
 77 and a review of the major applications can be found in *Randall et al.* [2016]. A second
 78 MMF² [*Tao et al.*, 2009] has been developed at Goddard with a different GCM [the
 79 Goddard Earth Observing System (GEOS) model] and a different CRM [the Goddard
 80 Cumulus Ensemble model (GCE)]. Recently, a new Goddard 4ICE (cloud ice, snow,
 81 graupel and hail) scheme was implemented into the GMMF [*Chern et al.*, 2016]. The
 82 4ICE scheme improves the GMMF-simulated cloud ice spatial patterns and amount as
 83 compared to CloudSat estimates. It also shows improved performance with respect to
 84 the land-ocean contrast in precipitating cloud frequencies and microphysics in relations
 85 to the TRMM products and results from a GCRM [*Matsui et al.*, 2016]. GMMF
 86 simulations with the improved 4ICE scheme were incorporated into a satellite-retrieval
 87 database for the cross-track scanning sensors of the Global Precipitation Measurement
 88 (GPM) constellation satellites [*Kidd et al.*, 2016].

89
 90 *Khairoutdinov and Randall* [2003] tested the sensitivity of their CRM (SAM) to
 91 domain size (from 512 to 9192 km) and horizontal resolution (from 250 m to 32 km).
 92 Their 20-member ensemble runs were forced by large-scale advective tendencies in
 93 temperature and water vapor from an intensive observation period conducted over
 94 Oklahoma in 1997 at the ARM/SGP (DOE Atmospheric Radiation Measurement
 95 Program / Southern Great Plains) site. They found that the mean simulation statistics

² It is called the Goddard MMF or GMMF.

96 had very little sensitivity to the model domain size. They also found that the simulated
97 hydrometeor-mixing rate and cloud fraction profiles had virtually no sensitivity to grid
98 resolution as long as it was finer than 4 km. Their conclusions are one of the main
99 reasons why nearly all MMFs applied a 4-km grid in their embedded CRMs (See Table
100 1).

101
102 The importance of mesoscale convective systems (MCSs) on tropical precipitation was
103 identified [Houze, 1982, 1989] and quantified from TRMM precipitation radar and
104 microwave imager retrievals [Nesbitt *et al.*, 2006] and CRMs [see Table 1 in Cotton *et al.*, 1995]. MCSs generate more than 50% of the rainfall in most tropical regions.
106 Typical MCSs have a horizontal scale of a few hundred kilometers. Johnson *et al.*
107 [2002] used large-scale advective tendencies for temperature and water vapor obtained
108 from TOGA COARE (the Tropical Ocean Global Atmosphere – Coupled Ocean
109 Atmosphere Response Experiment) to force the GCE. Their results indicated that a
110 domain size of at least 512 km is needed to adequately contain “meso-scale convective
111 features” and to replicate both the eastward and westward movements of the observed
112 precipitating systems. Tompkins [2000] and Petch and Gray [2001] also indicated the
113 importance of mesoscale organization in their TOGA COARE CRM simulations.
114 Computationally, it is still quite expensive to use a 512 km domain size with 1 or 2 km
115 grid spacing in the embedded CRMs of an MMF. In addition, Ooyama [2001] used a
116 two-dimensional non-hydrostatic model to test the sensitivity of an isolated convective
117 cloud and a squall line to resolution (1, 2 and 4 km). His results suggested that a

118 resolution of 1 km or less, or marginally 2 km, is needed to realistically simulate
119 precipitating clouds and squall lines.

120

121 Table 1 shows a list of MMF papers and their model configurations, such as their GCM
122 resolution, the resolution and number of grid points in their CRMs, and length of model
123 integration. Most MMFs used 32 or 64 grid points with 4 km grid spacing in their
124 embedded CRMs. Only a few MMF studies [e.g., *Marchand and Ackerman*, 2010;
125 *Pritchard et al.*, 2011] used 1 km grid spacing. Please see *Chern et al.* [2016] and
126 *Randall et al.* [2016] for a review of these MMF papers in terms of their development,
127 improvements and applications.

128

129 In this study, GMMF sensitivity tests were conducted to examine the impact of number
130 of CRM grids and their resolution on model simulations. Specifically, the physical
131 processes that can cause excessive rainfall over the West Pacific and other tropical
132 oceans are the focus of the study. The paper has the following organization. Section 2
133 describes the GMMF, the Goddard microphysical schemes, and sensitivity tests.
134 Section 3 shows the results of the numerical experiments assessing the impact of model
135 configuration on surface rainfall. Section 4 offers a summary and conclusions.

136

137 **2. Model description and numerical experiments**

138

139 *2.1 The Goddard MMF (GMMF)*

140

141 The GMMF used in this study is the same as in *Chern et al.* [2016]. Briefly, the moist
142 processes, radiation, and turbulence schemes in the GEOS global atmospheric model
143 have been replaced with a two-dimensional (x-z) GCE [*Tao et al.*, 2014]. The GEOS
144 model was configured to run with $2^\circ \times 2.5^\circ$ (latitude x longitude) horizontal grid
145 spacing with 48 vertical layers stretching from the surface to 0.4 hPa. In this study, a
146 series of simulations were carried out with differing numbers of GCE grid columns
147 (i.e., 32, 64, and 256) and grid spacing (i.e., 1, 2, and 4 km). All embedded GCEs have
148 44 vertical layers and time steps of 3, 6, and 12 seconds for model resolutions of 1, 2,
149 and 4 km, respectively. In the GMMF, the GCE is in a height coordinate, and the model
150 height does not change with time (different from SPCAM's approach). Therefore, the
151 vertical levels are slightly different between GEOS and GCE to ensure the model top
152 height in the GCE is lower than that of GEOS. Prescribed sea surface temperatures
153 (SSTs) from NOAA OI weekly SSTs [*Reynolds et al.*, 2007] were used, while the initial
154 atmospheric conditions were taken from the ECMWF ERA-Interim reanalysis [*Dee et*
155 *al.*, 2011] at 0000 UTC 1 December 2006. The first month was considered as spin-up,
156 and only results from 2007 and 2008 were depicted in this paper. In this study, the
157 surface fluxes are computed from the GCM grids based on the GCM's lowest-level
158 fields and are used as constant fluxes (horizontally uniform) in the embedded CRM.
159 The representation of convective momentum transport (CMT) in an MMF has been a
160 long-standing challenge due to the 2D nature of the embedded CRMs. The GMMF is
161 like other traditional MMFs in only considering the thermodynamic feedback.

162

Most CRM microphysical schemes include two liquid (cloud water and rain) and three classes of ice particles (cloud ice, snow and graupel or hail) [see Table 1 in *Tao et al.*, 2016]. However, graupel and hail can co-exist in real clouds. Therefore, the Goddard 3ICE scheme was improved by including both graupel and hail (called the Goddard 4ICE scheme, see *Lang et al.* [2014]). The Goddard 4ICE scheme was also implemented into the NASA Unified Weather Research and Forecasting model (NU-WRF), which significantly improved the simulation of heavy rainfall associated with a mid-latitude squall line [*Tao et al.*, 2016]. The 4ICE scheme improves the GCE and NU-WRF radar signatures in two ways: 1) it eliminates the occurrence of elevated reflectivity maxima (most likely via higher hail fall speeds) and still works well for less intense cases, and 2) with its ability to produce high reflectivity values, it eliminates the need for graupel and snow to produce those values, allowing for more “stable” snow/graupel size mappings and mappings better suited to produce reflectivity values with the highest occurrence. This 4ICE scheme is used in both GCE and GMMF for this study.

178

179 2.2 *Model configuration and sensitivity tests*

180

Table 2 lists four GMMF sensitivity tests. The first two sensitivity tests (M32 and M64) used 32 and 64 CRM grid columns with 4 km grid spacing, respectively. These model configurations are frequently used in MMF simulations (see Table 1). The next two sensitivity tests (M128 and M256) used 128 and 256 CRM grid columns with 2 and 1 km grid spacing, respectively. The embedded CRMs have an east-west orientation. Note that the M64, M128 and M256 configurations have the same domain

size (256 km), which is similar to the GEOS longitudinal grid spacing (2.5°). Most previous MMF studies (Table 1) used embedded CRMs with a domain size of 128 km and 4 km grid spacing, which matches and is the justification for the M32 simulation. It is worth noting that the majority of organized tropical convective systems are over 100 km in size [Nesbitt *et al.*, 2006]. These two tests are designed to examine whether simulated convection is more or less organized than the two tests with less grid columns.

In addition to the GMMF simulations, four CRM (GCE) simulations (i.e., C32, C64, C128 and C256 in Table 2) are conducted. The same CRM configurations used in the GMMF runs are used in these CRM simulations. Large-scale advective forcing in temperature and water vapor is used to derive these CRM simulations. These off-line (non interactive with GEOS) simulations are used to examine the sensitivity of CRM configurations on surface precipitation and the degree of convective organization.

3. Results

3.1 CRM simulations

The GCE is used to examine the sensitivity of stand-alone 2D CRM simulations without cloud-large scale interaction to horizontal resolution and domain size. The observed large-scale forcing in temperature and water vapor from 20 to 30 November 2011 during the Dynamics of the Madden-Julian Oscillation (DYNAMO, Yoneyama *et al.*, 2013) field campaign is used to drive the simulations (i.e., C32, C64, C128 and C256 case). Surface rainfall retrieved by the ground-based S-band dual-polarized (S-

212 POL) radar located at Gan Island was used to constrain the forcing. Since there was
 213 only a single sounding site at Gan Island, ECMWF global analyses were used to
 214 provide temperature, water vapor and wind profiles near the Gan site. Table 3 shows
 215 the convective, stratiform, and total rainfall, its stratiform percentage, temporal
 216 correlation as well as the domain mean rainfall bias for these four simulations. The
 217 convective and stratiform separation method considers the surface rainfall intensity,
 218 middle-level vertical velocity, and low-level cloud water (100% saturated with
 219 presence of cloud water). Please see *Tao et al.* [1993] and *Lang et al.* [2003] for more
 220 details on the separation method. All of the runs produced similar rainfall totals (from
 221 12.86 to 13.37 mm) in good agreement with the observed (13.03 mm). This is because
 222 the runs were all constrained by the prescribed large-scale advective forcing in
 223 temperature and water vapor.

224

225 The C32 and C64 runs both used the same 4-km grid spacing, but the C64 simulation
 226 had slightly more convective and stratiform rainfall (Table 3). The results also showed
 227 that both the C32 and C64 runs simulated the same 57% stratiform rainfall amount.
 228 The C128 and C256 cases both produced more convective but less stratiform rainfall
 229 and hence a slightly lower stratiform percentage (53%) than the C32 and C64 cases.
 230 The C256 experiment had the highest correlation (0.90) of all and a lower bias (0.23)
 231 than the C64 and C128 runs. The C32 simulation had the lowest correlation (0.73) and
 232 a negative bias compared to the others.

233

Figure 1 shows time series of the domain-mean rainfall for the C32, C64, C128 and C256 simulations. All four runs capture the observed temporal variation in rainfall, especially the heavy rainfall events (i.e., on November 23, 24, 25, 26, 27 and 28). However, the C32 run generally overestimates the peak intensity of these heavy rainfall events while underestimating their life span compared to the observations and other simulations. The C64 and C128 runs are both better than the C32 case in this regard with C128 being slightly better than the C64 during the first 4 days of model integration. The C256 simulation, however, clearly shows the best agreement with the observed temporal variation in domain mean surface rainfall in agreement with the high correlation and low bias shown in Table 3.

244

Hovmoller diagrams of model-simulated hourly rainfall for the C32, C64, C128 and C256 simulations are shown in Fig. 2. The C32 run produces short-lived, isolated convection with large rainfall intensities (especially between November 20-21 and November 25-28) compared to the other runs. Its simulated domain-mean rainfall period is also shorter than the other cases as shown in the Fig. 1a. The C256 simulation has more long-lived organized convection, and its simulated domain-mean rainfall is in very good agreement with the observed as shown in Fig. 1d. In addition, the C256 run produces finer, more-detailed structures than the C32. The C128 run has slightly more long-lived, organized convection than does C64 between November 25 and November 27 (see Fig. 2 and Fig. 1c) and slightly better correlation overall (Table 3).

255

Figure 3 shows vertical cross sections of simulated radar reflectivity from the four CRM simulations. In general, more complex cloud structures are seen in the C256 (1-km resolution) and C128 (2-km resolution) simulation. Convective cell structures appear broader for the C32 and C64 simulations (see Figs. 3a and b). These results are in good agreement with Ooyama [2001]. The time series of maximum vertical velocity and maximum radar reflectivity are also examined (not shown). The peak intensity of radar reflectivity is about 45-50 dBZ in all GMMF experiments (see Fig 3). These values are located beneath the melting layer. The maximum updraft (grid point value) is stronger (weaker) in the high (low)-resolution case as expected. For example, the maximum updraft is about 8 m s^{-1} in the M32 configuration but reaches over 12 m s^{-1} in the M256 case. Another difference is that stronger updrafts last longer (shorter) in the M256 (M32) case as multi-convective cores are simulated in M256 (see Fig. 3). This result is consistent with the rainfall (Fig. 1).

269

270 3.2 GMMF simulations

271

GMMF simulations were conducted for two years, January 1, 2007 to December 31, 2008. These same two years were used to compare the GMMF M32 simulation with CloudSat products in Chern *et al.* [2016]. In this paper, GMMF-simulated rainfall characteristics will be compared for different model configurations. The Global Precipitation Climatology Project (GPCP) [Adler *et al.*, 2003] and two Tropical Rainfall Measuring Mission (TRMM) [Simpson *et al.*, 1996] products [Huffman *et al.*, 2007, 2010] are used to evaluate model performance. The GPCP data has global

279 coverage at 2.5° resolution, the TRMM 3B43 merged product covers from 50°S to 50°N
 280 at 0.25° resolution, and the TRMM 3A25 Precipitation Radar (PR) gridded product
 281 covers from 38°S to 38°N at 0.5° resolution. All datasets are averaged to the model
 282 grids at 2.0° x 2.5° resolution for comparison.

283

284 The GCE model configurations used in the M32, M64, M128 and M256 experiments
 285 are the same as those in the C32, C64, C128 and C256 simulations, respectively, except
 286 now the GCE models can interact with the global circulation model (GEOS).
 287 Therefore, they do not have the same large-scale advective forcing (or vertical shear of
 288 horizontal wind) as their counterparts. Figure 4 shows the two-year mean surface
 289 rainfall simulated in the M32, M64, M128 and M256 runs. The satellite surface rainfall
 290 estimates from the TRMM 3B42 and GPCP products are also shown in Fig. 4 for
 291 comparison. All of the MMF-simulated rainfall patterns are quite similar to each other
 292 and to the satellite retrievals. For example, the minimum rain regions off the west
 293 coasts of North and South America and over subtropical Africa and the Atlantic are
 294 captured by all four simulations. In addition, four major rainfall features/regions, such
 295 as the Intertropical Convergence Zone (ITCZ), South Pacific Convergence Zone
 296 (SPCZ), Indian Ocean and West Atlantic are also well captured by the GMMF runs.
 297 However, all four runs still simulate more rainfall than is estimated by satellite in these
 298 major rainfall regions. However, the results clearly indicate that the M128 and M256
 299 runs produce less total rainfall over these regions than do the M32 and M64 runs,
 300 making them in better agreement with the satellite observations. Figure 5 shows the
 301 zonal mean rainfall differences between the four GMMF simulations and GPCP and

302 TRMM. The biggest differences between the simulations and satellites observations
 303 are over the Tropics. The maximum zonal mean bias for the M256 simulation is
 304 noticeably less than for the M32 (1.4 mm day⁻¹ vs. 2.2 mm day⁻¹ compared to GPCP
 305 and 1.9 mm day⁻¹ vs. 2.8 mm day⁻¹ compared to TRMM in the Tropics). Overall, the
 306 M256 run has the least difference in (zonal-mean) rainfall compared to both TRMM
 307 and GPCP. The M64 and M128 runs also have smaller differences than does the M32.

308

309 The total rainfall amount, its bias, root mean square error (RMSE) and correlation for
 310 the four GMMF experiments are shown in Table 4. The convective and stratiform
 311 rainfall amount and stratiform percentage from each run are also shown. The M256
 312 run has the lowest total rainfall amount, 2.83 (3.12) mm/day, the smallest bias 0.17
 313 (0.22) and RMSE 1.37 (1.42), and the highest spatial correlation 0.842 (0.857)
 314 compared to GPCP (TRMM) among all runs. In contrast, the M32 simulation has the
 315 largest total rainfall amount, 2.93 (3.27) mm/day, the largest bias 0.27 (0.36) and
 316 RMSE 1.74 (1.85) as well as the smallest correlation 0.817 (0.825) of the runs relative
 317 to GPCP (TRMM). The M64 simulation has a better bias, RMSE and correlation than
 318 the M32. The M128 run produces the second best results and implies that CRMs with
 319 128 grid points could be embedded into the GMMF and still achieve better agreement
 320 (reduced bias/RMSE and increased correlation) with observed rainfall than the current
 321 default setup.

322

323 The domain size of the CRM is typically chosen to be equal to or smaller than the
 324 parent GCM's grid spacing (~2 degree) in an MMF setup such as with the M32, M64,

325 M128, and M256 experiments. However, a CRM domain size of 256 km (~2 degrees)
326 may be smaller than that necessary (i.e., 512 km) to adequately simulate tropical MCSs
327 as suggested from previous stand-alone CRM simulations [*Tompkins, 2000; Johnson*
328 *et al., 2002; Petch and Gray, 2001*]. Therefore, an additional M128 configuration with
329 4 km grid spacing (i.e., a domain size of 512 km) was carried out; its global mean
330 precipitation (not shown) has a bias/RMSE/correlation of 0.21/1.47/0.82, which are
331 better than the GMMF runs (i.e., M32 and M64) with the same CRM grid spacing but
332 smaller domains (i.e., 128 km and 256km). This result indicates that expanding the
333 CRM domain to 2 times that of a typical parent GCM grid box (2 x 2.5 degrees) can
334 allow for more realistic MCS circulations and thereby reduce the artificial impacts of
335 cyclic boundary conditions. However, the precipitation statistics for this additional test
336 (i.e., 512 km domain size) are slightly worse than the M128 run with a higher resolution
337 but smaller domain.

338

339 The M32 and M64 simulations typically produce one isolated cloud or cloud system as
340 compared to the M128 and M256, which tend to produce more organized multi-cellar
341 convective systems (see Fig. 6). For example, Fig. 6(d) shows an organized MCS with
342 strong updrafts at the leading edge of the system and weaker updraft trailing behind
343 (associated with a decaying convective cell). The updrafts are also stronger and
344 penetrate to higher altitudes than those in the M32 and M64 runs (Figs. 6a and b). Note
345 that propagating convective cell(s)/system(s) exit from one lateral boundary and re-
346 enter on the other side due to the cyclic lateral boundary conditions.

347

348 The GMMF results are quite consistent with those from the uncoupled GCE runs. For
349 example, the runs with 256 grid points (M256 and C256) have a low total rainfall bias
350 and high spatial correlation compared to those with fewer grid points. In addition, the
351 M256 and C256 runs simulate more organized MCSs compared to the M32 and C32.
352 Both the M128 and C128 runs also have better bias results and correlations compared
353 to their M64 and C64 counterparts. Overall, for both the GMMF and GCE model,
354 simulations with the least number of model grid points have the worst performance in
355 terms of simulated rainfall (Figs. 1, 4 and 5).

356

357 All of the GCE and GMMF simulations produce a large stratiform rain percentage
358 (from 51 to 63%, see Tables 3 and 4). The M32 and M64 runs simulated lower
359 stratiform rain fractions, 55 and 51%, respectively, than the M128 and M256. These
360 results are consistent with the more organized clouds/cloud systems in the M128 and
361 M256 simulations. On the other hand, the C128 and C256 runs produced 4% lower
362 stratiform fractions than the C32 and C64 (Table 3) even though there are more
363 organized convective systems in the C128 and C256 simulations (Fig. 3). This result
364 is one of the differences between the GMMF and GCE simulations. Note that identical
365 large-scale advective forcing with nudged horizontal winds was used to drive the un-
366 coupled GCE experiments. Also, *Lang et al.* [2003] compared different convective-
367 stratiform separation methods in the GCE model. Their results showed that the GCE-
368 based (used in this paper) separation method could produce a higher stratiform (or less
369 convective) fraction compared to the radar reflectivity-based method [*Steiner*, 1995].

370

371 Only one MMF study [*Cheng and Xu*, 2011] showed that simulated surface rainfall
 372 (SPCAM3.5) was under-predicted compared to observations [*Legates and Willmott*,
 373 1990; see Fig. 11 in *Cheng and Xu*, 2011]. However, in that study, the results were not
 374 compared with TRMM and/or GPCP as in other MMF studies (shown in Table 1).
 375 *Marchand and Ackerman* [2010] conducted three SPCAM simulations with different
 376 horizontal resolutions/ vertical levels (i.e., 4 km/ L26, 1km/ L26, and 1km/ L52,
 377 respectively). The 1-km simulations were only integrated for one month (November
 378 2006). Their analysis only focused on cloud amount (not surface rainfall); they found
 379 the 1km/ L52 setup modestly improved the MMF-simulated low-cloud cover.
 380 *Pritchard et al.* [2014] also examined the impact of grid spacing on MJO dynamics in
 381 the SPCAM. Three CRM configurations (128 km long with 32 columns, 64 km long
 382 with 16 columns and 32 km long with 8 columns) were integrated in SPCAM for a ten-
 383 year period (1980-1990). Their three simulations produced less rainfall on the equator
 384 and too much off of it (i.e., North Indian Ocean, Bay of Bengal, and northwestern
 385 tropical Pacific). The two configurations with reduced CRM domain sizes produced
 386 more rainfall on the Equator and slightly less rainfall in the Indian Ocean and SPCZ
 387 (see Fig. 7 in their paper). *Pritchard et al.*'s results differ from this study as all of the
 388 GMMF runs produce too much rainfall along the Equatorial ITCZ and over the SPCZ
 389 and Indian Ocean. The differences could be caused by differences in the physics as
 390 well as the configuration tests between their study and this one.

391

392 3.3 Process diagnostics

393

394 *Luo and Stephens* [2006] examined SPCAM simulations and suggested that a large
 395 convection-wind-evaporation feedback, partially caused by the two-dimensional
 396 geometry of the embedded CRMs in the global model, could cause the positive surface
 397 rainfall bias. *Kim et al.* [2011] examined the relationships between intra-seasonal
 398 variability (ISV) and precipitation bias in AGCMs. They also found that evaporation
 399 is larger in the stronger ISV models than in the weak ones. This result is consistent
 400 with the feedback suggested by *Luo and Stephens* [2006]. However, they also found
 401 this feedback occurs in models with cumulus parameterization. They suggested that
 402 other physical processes (i.e., air-sea interaction using ocean models) might cause this
 403 positive precipitation bias.

404

405 Table 5 shows the evaporation rate (or latent heat flux) in mm day^{-1} from the four
 406 GMMF experiments. It also shows the surface rainfall rate for comparison. The
 407 observed precipitation rate, the evaporation rate over ocean, and the evaporation rate
 408 over land come from GPCP, OAFflux (Objectively Analyzed air-sea Fluxes; *Yu and*
 409 *Weller*, 2007), and FLUXNET [*Baldocchi et al.*, 2001], respectively. The OAFflux
 410 project uses objective analysis to synthesize measurements/estimates from various
 411 sources and provides surface fluxes and flux-related surface meteorology globally for
 412 ice-free oceans. FLUXNET is a gridded flux product from a global network of more
 413 than 500 micrometeorological tower sites. This gridded product is useful for model
 414 validation from local to global scales [*Jung et al.*, 2009; *Blyth et al.*, 2010]. All GMMF
 415 simulations in general overestimate surface precipitation and evaporation rates over
 416 ocean but underestimate them over land. The results show that a higher evaporation

417 rate is associated with more surface rainfall over oceans. For example, the M32 and
 418 M64 runs show more surface rainfall and higher surface evaporation rates than those
 419 for the M128 and 256 runs. The surface evaporation rate is much lower over the deep
 420 Tropics (15° S to 15° N) for the M128 and M256 runs than for the M32 and M64. On
 421 the other hand, more surface rainfall over land in the M128 and M256 runs corresponds
 422 to more evaporation over land. However, the differences between the M32 and M64
 423 runs and the M128 and M256 runs are smaller over land than they are over ocean.

424

425 Figure 7 shows mean surface evaporation (in mm day^{-1} for comparison with the surface
 426 rainfall) for the M32, M64, M128 and M256 simulations as well as for the combination
 427 of the OAFlux and FLUXNET products for comparison. The results show a very
 428 similar spatial distribution for all four GMMF runs. Peak evaporation is larger in the
 429 M32 simulation than in the other three runs. These regional maxima are smaller in the
 430 M256 run than those in the M64 and M128 runs. In terms of the zonal mean
 431 evaporation bias (Fig. 7f), the M32 simulation clearly has a higher evaporation bias
 432 from 15° S to 15° N than the other simulations. It is worth noting that the areas of
 433 largest surface evaporation are not co-located with the areas of highest surface rainfall
 434 (Fig. 4). For example, the areas of large surface evaporation are located well south and
 435 well north of the ITCZ and West Atlantic. Also, large surface evaporation occurs south
 436 of the large surface rainfall over the Indian Ocean. This suggests that local surface
 437 latent heat flux is not a major physical process with regard to the precipitation bias.

438

Low-level water vapor flux convergence, which is the integral of water vapor flux convergence from the surface to 700 hPa, was calculated to examine its relation to surface rainfall (Fig. 8). The results show that all of the simulations have very similar spatial patterns that are also similar to their surface rainfall patterns. Large values of water vapor flux convergence are co-located with the large surface rainfall regions. For example, strong water vapor flux convergence occurs over the ITCZ, SPCZ, Indian Ocean and West Atlantic where the larger rainfall occurs (see Fig. 5). In addition, low-level water vapor flux convergence over land (South America and Africa) also coincides with areas of large surface rainfall. The results indicate that there is a close relationship between low-level water vapor flux convergence and surface rainfall. Figure 8 also shows that the M32 (M256) simulation has the largest (smallest) low-level water vapor flux convergence among all four runs. Low-level water vapor flux convergence is mainly controlled by the large-scale circulation.

Dynamic processes are also therefore examined to explain the differences between these runs. Figure 9 shows annual average, zonal mean meridional mass stream function values and mean vertical pressure velocity from the M32 and M256 simulations. The meridional mass stream function, Ψ , is expressed as

$$\Psi = \frac{2\rho a \cos(\varphi)}{g} \int_p^{p_s} v dp,$$

where a is the Earth's radius, g is the gravitational acceleration, φ is the latitude, p_s is the surface pressure, p is the pressure, and v is the zonal average meridional wind. The stream function values are assumed to be zero at the top and bottom boundaries to ensure mass conservation and a steady state solution to the continuity equation. Positive

462 and negative stream function values represent counterclockwise and clockwise
 463 circulations, respectively, and their amplitude measures the strength of the circulation.
 464 The M32 and M256 average stream functions (Fig. 9) both show a roughly symmetric
 465 two-cell structure with a mutual ascending branch located north ($\sim 5^\circ$ N) of the equator.
 466 The minimum/maximum values of mass stream function are $-11.92/10.39$ ($\times 10^{10}$ kg s⁻¹)
 467 ¹) and $-11.25/9.10$ ($\times 10^{10}$ kg s⁻¹) for the M32 and M256 simulations, respectively.
 468 These results indicate that the strength of both the southern and northern Hadley
 469 circulations in the M32 run are stronger than those in the M256. A stronger Hadley
 470 circulation in M32 allows for stronger low-level water vapor flux transport from the
 471 sub-tropics to the Tropics as shown in Fig. 8.

472

473 The vertical velocity is clearly much stronger in the M32 simulation than in the M256
 474 with M64 and M128 in between for both tropical ocean and land regions (Figs. 10a and
 475 b). There is a larger difference over ocean than over land. These results are consistent
 476 with the rainfall (Fig. 4 and Table 5) with the M32 simulation having more surface
 477 rainfall than the M256. Figure 10 also shows the vertical velocity in the subtropics
 478 over ocean and land. There is stronger subsidence in the M32 run than in the M256
 479 with M64 and M128 again in between for both land and ocean, which is consistent with
 480 the subtropical surface rainfall patterns as well. These results also suggest that the
 481 stronger subsidence in the sub-tropics could allow more warming and drying in the
 482 M32 run and consequently more surface fluxes (i.e., evaporation).

483

484 *Donner et al.* [2001] examined the impact of mesoscale effects in an atmospheric GCM.
 485 They incorporated both convective-scale vertical velocity and mesoscale effects into a
 486 cumulus parameterization scheme based on mass fluxes and found that the results were
 487 in better agreement with satellite observations (i.e., TRMM and NVAP – the NASA
 488 Water Vapor Project) if both convective and mesoscale effects are included. Their
 489 results also indicated that mass fluxes are smaller when the mesoscale component is
 490 included. This is in good agreement with our current results. *Donner et al.* [2001] did
 491 not discuss the mesoscale effects on surface rainfall.

492

493 The impact of mesoscale precipitation systems within global circulation models has
 494 been examined. For example, *Schumacher et al.* [2004] studied the tropical dynamic
 495 response to latent heating estimates derived from the TRMM precipitation radar within
 496 an idealized simulation. Their results showed that stratiform fraction plays an
 497 important role in shaping the structure of the large-scale tropical circulation response
 498 to precipitating cloud systems. Cold pools (typically associated with convective
 499 systems) were considered in *Del Genio et al.* [2015] and do have an impact on the
 500 Madden-Julian oscillation (MJO) simulations (but entrainment from convection can
 501 determine whether or not a realistic MJO can be simulated). But, they have more
 502 impact on upper-level cloudiness, which interacts with radiative heating [*Del Genio et*
 503 *al.*, 2015]. Their model simulations were 30 days long.

504

505 3.4 *Sensitivity to reduced evaporative fluxes*

506

507 *Kim et al.* [2011] have examined the relationship between intraseasonal variability and
508 mean state bias in several GCMs as well as the relationship between surface
509 evaporative fluxes and precipitation. Their results showed a positive correlation
510 between evaporative fluxes and precipitation. The models with more evaporative
511 fluxes simulated more precipitation. They suggested that the over-estimated surface
512 rainfall in GCMs is likely due to the prescribed SST lower boundary.

513

514 To examine the role of air-sea interaction within climate simulation, *Stan et al.* [2010]
515 coupled the SPCAM to a full-physics ocean model, POP (the Parallel Ocean Program).
516 They found the coupled model eliminated excessive precipitation over the western
517 Pacific during summer and produced a better simulation of the Asian monsoon
518 circulation than the uncoupled SPCAM. However, this improved simulation could also
519 be due to the fact that the SSTs could deviate from observations in the coupled model.
520 *Stan et al.* [2010] also showed there were mean SST cold biases of 1-2 K with an RMSE
521 value of 2 K [*Randall et al.*, 2016] in many locations. These cold biases must have a
522 large impact on the simulated surface evaporation, precipitation and circulation
523 patterns. To provide a more realistic air-sea interaction, *Benedict and Randall* [2011]
524 coupled the SP-CAM to a simplified slab ocean model that was constrained to observed
525 climatology. Although the annual mean SST variations were only a few tenths of a
526 degree from the observed SSTs, they found the organization and eastward propagation
527 of the MJO to be more realistic than in the uncoupled SP-CAM. However, the
528 excessive annual mean precipitation in the tropics and western Pacific still existed.

529

530 To investigate the impact of SST cold biases of 1-2 K on surface evaporation,
 531 precipitation pattern, and the Hadley circulation, a simple sensitivity test was conducted
 532 using the M32 configuration but with the SSTs reduced (in °C) by 5%. Surface
 533 evaporation is reduced compared to the control (M32) run (Fig. 11a and Fig. 7b),
 534 lowering both the bias and RMSE (bias from 0.477 to 0.319; RMSE from 1.017 to
 535 0.782), while increasing the correlation from 0.816 to 0.937. These statistics are quite
 536 comparable to the M256 simulation (i.e., a 0.345 bias, an RMSE of 0.781, and a 0.939
 537 correlation). Nevertheless, the spatial distribution between this run and the M32 run is
 538 quite similar. As surface evaporation is reduced, surface rainfall is also reduced
 539 compared to the M32 run (Fig. 11b and Fig. 4c) in better agreement with observations.
 540 The bias/RMSE/CORR for precipitation against GPCP observations is
 541 0.131/1.563/0.816 for the reduced SST scenario. The results are again quite similar to
 542 those for the M256 simulation (see Table 4). The zonal meridional mass stream
 543 function (Fig. 11d) has minimum/maximum values of -12.99/9.79 ($\times 10^{10} \text{ kg s}^{-1}$), which
 544 are smaller than those [-11.92/10.39 ($\times 10^{10} \text{ kg s}^{-1}$)] for the M32 experiment (Fig. 9a).
 545 This demonstrates that the southern (northern) branch of the Hadley circulation is
 546 stronger (weaker) in the sensitivity test versus the control. The reduction of tropical
 547 precipitation in the SST-5% experiment is associated with smaller low-level moisture
 548 flux convergence (Fig. 11c). This can be attributed mainly to a drier lower atmosphere
 549 as a result of weaker surface latent heat fluxes in the SST-5% sensitivity experiment.
 550 These results show that the SST cold biases in a coupled model could have a significant
 551 influence on the large-scale circulation and precipitation distributions through

552 convection-wind-evaporation feedback [*Luo and Stephens, 2006*] in a
 553 superparameterization model system.

554

555 **4. Summary and conclusions**

556

557 Almost all MMFs (including the GMMF) have used 32 or 64 grid points with 4 km
 558 grid spacing in their embedded CRMs and overestimated precipitation (surface rainfall)
 559 in the Tropics. In this study, the major physical processes are examined and identified
 560 that cause the overestimated rainfall in the GMMF. Both GCE and GMMF simulations
 561 are conducted with different numbers of CRM grid points and spacing. In addition, a
 562 sensitivity test with the GMMF using reduced SSTs was conducted. The main results
 563 from this modeling study are as follows:

564

- 565 • Overall, the GCE setup with the most grid points (i.e., C256 case) and highest
 566 resolution (1 km) has the lowest bias and highest correlation in terms of surface
 567 rainfall. In contrast, the GCE setup with the fewest grid points (i.e., the C32
 568 configuration) and lower resolution (4 km) has the lowest correlation with surface
 569 rainfall. The other two simulations (i.e., C64 and C128) have biases and
 570 correlations in between the C256 and C32 runs.
- 571 • The GCE setup with more grid points (C256) produces more long-lived, organized
 572 convective systems and a temporal rainfall variation in very good agreement with
 573 observations. This result is in good agreement with previous CRM simulations that
 574 a larger domain is required to better simulate organized convection [i.e., *Johnson*
 575 *et al.*, 2002; *Tompkins*, 2000; *Petch and Gray*, 2001].

- 576 • The GCE configuration with the least grid points (C32) simulates short-lived,
577 isolated convection. Its simulated domain-mean rainfall also lasts for a shorter time
578 period and is stronger compared to the other runs and to observations.
- 579 • Overall, the GMMF simulations show very similar surface rainfall patterns and
580 capture the major weather phenomena, such as a single ITCZ and SPCZ and large
581 rainfall over the Indian Ocean, S. America and Eastern Atlantic. However, all of
582 the GMMF simulations over-estimated the total rainfall amount compared to
583 satellite estimates from TRMM and GPCP.
- 584 • However, the GMMF with more CRM grid points and higher resolution (M256)
585 has a lower bias, smaller RMSE and higher correlation versus surface rainfall
586 compared to those with fewer grid points and lower resolution (i.e., M32, M64 and
587 M128). Overall, the M256 and M128 simulations are in better agreement with
588 observations than the M32 and M64.
- 589 • The M256 simulation produced more organized convective systems than the M32
590 and M64 with the M32 setup resulting in more isolated convection. These GMMF
591 results are consistent with the GCE model (non-coupled) simulations.
- 592 • The GMMF simulations indicate that convection-wind-evaporation feedback is a
593 key process for tropical precipitation. Globally, more (less) surface evaporation
594 produces more (less) surface rainfall. This result is in good agreement with
595 previous model results [*Luo and Stephens, 2006* and *Kim et al., 2001*]. However,
596 maximum surface evaporation occurs in sub-tropical regions. It is the large-scale
597 low-level circulation that transports the moisture from the subtropics to the tropical
598 ITCZs and SPCZ where the heavy rainfall occurs.

- 599 • The mean vertical velocity in the tropical region is weaker (stronger) for the M256
600 (M32) configuration. This is consistent with the results of *Donner et al.* [2001]
601 wherein mass fluxes are stronger when the mesoscale effect is not considered in the
602 cumulus parameterization.
- 603 • The stronger upward motion in the Tropics can allow stronger subsidence in the
604 sub-tropics. The warm, dry air associated with the subsidence that can then allow
605 larger surface evaporation..
- 606 • The upward motion in the Tropics also affects the Hadley circulation. A stronger
607 (weaker) Hadley circulation allows more (less) large-scale low-level water vapor
608 to be transported from the subtropics to the Tropics.
- 609 • Surface evaporation is weaker in the GMMF sensitivity test wherein SSTs were
610 reduced by 5% compared to the control simulation (M32). Consequently, the
611 tropical rainfall is also reduced due to smaller low-level moisture flux convergence
612 associated with a drier low atmosphere. These results suggest that the cold SST
613 biases in a coupled model can play an important role in the global rainfall
614 distribution.

615

616 One of the key findings in this paper is that MCSs can be simulated in both the GCE
617 and the embedded GCEs in the GMMF. But, it requires a relatively large number of
618 CRM grid points. For example, the GMMF M256 simulation needs much more
619 computation resources compared to the M32. Its computational requirement is similar
620 to a GCRM at ~10 km grid spacing. The next step would be to compare the

621 performance of the M256 configuration with the 7-km GEOS5 model (almost all global
 622 cloud-permitting models do not use 1 km grids, but more typically 3.5, 7 and 14 km).

623

624 One of the major limitations of MMFs is the use of a 2D CRM with cyclic lateral
 625 boundary conditions. Another limitation is that the MMF-embedded CRM zonal
 626 momentum is usually nudged to the large-scale model's momentum. Both could
 627 directly affect the large-scale organization of convection [*Moncrieff*, 2004]. For
 628 example, only one type of MCS (squall line) can be simulated by a 2D CRM. In
 629 addition, horizontal momentum could be counter-gradient for some types of convective
 630 organization [*LeMone et al.*, 1984; *Soong and Tao*, 1984; *Moncrieff*, 2004]. Only two
 631 recent MMFs (*Tulich*, [2015] and *Cheng and Xu*, [2014]) have considered the
 632 convective momentum transport (CMT). Both approaches utilize the low-level
 633 (surface to 4 km level) GCM wind shear to determine the orientation of the 2D CRM.
 634 For example, the orientation of the CRM can be perpendicular to the shear for
 635 organized (deep) convection or parallel to it for shallow clouds. However, the GCM
 636 resolution is quite coarse and the low-level wind shear may not be a good indicator of
 637 the convective organization. Nevertheless, the inclusion of CMT does improve the
 638 horizontal distribution of surface rainfall but not its total amount (see Fig. 16 in *Tulich*,
 639 [2015] and Fig. 1 *Cheng and Xu*, [2014]). This topic is an on-going area of research
 640 and is beyond the scope of this paper.

641 5. Acknowledgments

642

643 The GCE and GMMF models are mainly supported by the NASA Precipitation
 644 Measurement Mission (PMM) and the NASA Modeling, Analysis, and Prediction

(MAP) Program, respectively. The authors are grateful to Drs. Ramesh Kakar and David B. Considine at NASA headquarters for their support of this research and to Mr. Stephen Lang for carefully proofing the manuscript. We also thank Dr. M. Moncrieff and two anonymous reviewers for their constructive comments that improved this paper significantly.

650

Acknowledgment is also made to the NASA Goddard Space Flight Center and NASA Ames Research Center computing facilities and to Dr. Tsengdar Lee at NASA HQ for the computational resources used in this research. The results shown in section 3.1 were mainly produced by Mr. Sung-Yoon Kim and Dr. Myong-In Lee at the School of Urban and Environmental Engineering, Ulsan National Institute of Science & Technology (UNIST), Republic of Korea. The model outputs used in this study are available upon request from wei-kuo.tao-1@nasa.gov. The GPCP and TRMM datasets used in this study are accessible from <http://precip.gsfc.nasa.gov>.

659

660 **6. References**

661

Adler, R. F., et al. (2003), The version 2 Global Precipitation Climatology Project (GPCP) monthly precipitation analysis (1979-present), *J. Hydrometeorol.*, 4, 1147-1167, doi:10.1175/1525-7541(2003)004<1147:TVGPCP>2.0.CO;2.

Baldocchi, D., et al. (2001), FLUXNET: A new tool to study the temporal and spatial variability of ecosystem-scale carbon dioxide, water vapor, and energy flux densities, *Bull. Am. Meteorol. Soc.*, 82, 2415-2434.

Benedict, J. J., and D. A. Randall (2009), Structure of the Madden-Julian oscillation in

669 the superparameterized CAM, *J. Atmos. Sci.*, *66*, 3277-3296,
 670 doi:10.1175/2009JAS3030.1.

671 Benedict, J. J., and D. A. Randall (2011), Impacts of idealized air-sea coupling on
 672 Madden-Julian oscillation structure in the superparameterized CAM, *J. Atmos. Sci.*,
 673 *68*, 1990-2008, doi:10.1175/JAS-D-11-04.1.

674 Blyth, E., J. Gash, A. Lloyd, M. Pryor, G. P. Weedon, and J. Shuttleworth (2010),
 675 Evaluating the JULES land surface model energy fluxes using FLUXNET data, *J.*
 676 *Hydrometeor.*, *11*, 509-519, doi: 10.1175/2009JHM1183.1.

677 Cheng, A., and K.-M. Xu (2011), Improved low-cloud simulation from a multiscale
 678 modeling framework with a third-order turbulence closure in its cloud-resolving
 679 model component, *J. Geophys. Res.-Atmos.*, *116*, D14101,
 680 doi:10.1029/2010JD015362.

681 Cheng, A., and K.-M. Xu (2014), An explicit representation of vertical momentum
 682 transport in a multiscale modeling framework through its 2-D cloud-resolving
 683 model component, *J. Geophys. Res.-Atmos.*, *119*, 2356–2374,
 684 doi:10.1002/2013JD021078.

685 Chern, J.-D., W.-K. Tao, S. E. Lang, T. Matsui, J.-L. F. Li, K. I. Mohr, G. M.
 686 Skofronick-Jackson, and C. D. Peters-Lidard (2016), Performance of the Goddard
 687 multiscale modeling framework with Goddard ice microphysical schemes, *J. Adv.*
 688 *Model. Earth Syst.*, *7*, doi:[10.1002/2015MS000469](https://doi.org/10.1002/2015MS000469).

689 Cotton, W., G. D. Alexander, R. Hertenstein, R. L. Walko, R. L. McAnelly, and M.
690 Nicholls (1995), Cloud venting: A review and some new global annual estimates.
691 *Earth Sci. Rev.*, 39, 169-206.

692 Dee, D. P., et al. (2011), The ERA-Interim reanalysis: configuration and performance
693 of the data assimilation system, *Q. J. R. Meteorol. Soc.*, 137, 553–597,
694 doi:10.1002/qj.828

695 Del Genio, A. D., J. Wu, A. B. Wolf, Y. Chen, M.-S. Yao, and D. Kim (2015),
696 Constraints on cumulus parameterization from simulations of observed MJO
697 events, *J. Clim.*, 28, 6419-6442, doi: 10.1175/JCLI-D-14-00832.1.

698 DeMott, C. A., D. A. Randall, and M. Khairoutdinov (2007), Convective precipitation
699 variability as a tool for general circulation model analysis, *J. Clim.*, 20, 91-112,
700 doi:10.1175/JCLI3991.1.

701 DeMott, C. A., D. A. Randall, and M. Khairoutdinov (2010), Implied ocean heat
702 transports in the standard and superparameterized Community Atmospheric
703 Models, *J. Clim.*, 23, 1908-1928. doi: 10.1175/2009JCLI2987.1

704 DeMott, C. A., C. Stan, D. A. Randall, J. L. Kinter III, and M. Khairoutdinov (2011),
705 The Asian monsoon in the super-parameterized CCSM and its relationship to
706 tropical wave activity, *J. Clim.*, 24, 5134-5156, doi:10.1175/2011JCLI4202.1.

707 DeMott, C. A., C. Stan, and D. A. Randall (2013), Northward propagation mechanisms
708 of the boreal summer intraseasonal oscillation in the ERA-Interim and SP-CCSM,
709 *J. Clim.*, 26, 1973-1992, doi: 10.1175/JCLI-D-12-00191.1.

710 Dirmeyer, P. A., et al., (2012), Simulating the diurnal cycle of rainfall in global climate
711 models: resolution versus parameterization, *Clim. Dyn.*, 39, 399–418,

- 712 doi:10.1007/s00382-011-1127-9.
- 713 Donner, L. J., C. J. Seman, R. S. Hemler, and S. Fan (2001), A cumulus
 714 parameterization including mass fluxes, convective vertical velocities, and
 715 mesoscale effects: Thermodynamic and hydrological aspects in a general
 716 circulation model, *J. Clim.*, *14*, 3444–3463.
- 717 Goswami, B. B., N. J. Mani, P. Mukhopadhyay, D. E. Waliser, J. J. Benedict, E. D.
 718 Maloney, M. Khairoutdinov, and B. N. Goswami (2011), Monsoon intraseasonal
 719 oscillations as simulated by the superparameterized Community Atmosphere
 720 Model, *J. Geophys. Res.*, *116*, D22104, doi:10.1029/2011JD015948.
- 721 Goswami, B. B., P. Mukhopadhyay, M. Khairoutdinov, and B. N. Goswami (2013),
 722 Simulation of Indian summer monsoon intraseasonal oscillations in a
 723 superparameterized coupled climate model: need to improve the embedded cloud
 724 resolving model, *Clim. Dyn.*, *41*, 1497-1507, doi:10.1007/s00382-012-1563-1.
- 725 Grabowski, W. W., and P. K. Smolarkiewicz (1999), CRCP: a Cloud Resolving
 726 Convection Parameterization for modeling the tropical convecting atmosphere,
 727 *Physica D*, *133*, 171-178.
- 728 Houze, R. A. Jr. (1982), Cloud clusters and large-scale vertical motions in the tropics,
 729 *J. Meteorol. Soc. Jpn.*, *60*, 396-409.
- 730 Houze, R. A. Jr. (1989), Observed structure of mesoscale convective systems and
 731 implications for large-scale heating, *Q. J. R. Meteorol. Soc.*, *115*, 425-461.
- 732 Huffman, G. J., et al. (2007), The TRMM Multi-satellite Precipitation Analysis: Quasi-
 733 global, multi-year, combined-sensor precipitation estimates at fine scale, *J.*
 734 *Hydrometeorol.*, *8*, 38-55, doi:10.1175/JHM560.1.

- 735 Huffman, G. J., R. F. Adler, D. T. Bolvin, and E. J. Nelkin (2010), The TRMM Multi-
 736 satellite Precipitation Analysis (TMPA), in *Satellite Rainfall Applications for*
 737 *Surface Hydrology*, edited by F. Hossain and M. Gebremichael, pp. 3-22, Springer
 738 Verlag, ISBN: 978-90-481-2914-0.
- 739 Johnson, D. E., W.-K. Tao, J. Simpson, and C.-H. Sui (2002), A study of the response
 740 of deep tropical clouds to large-scale thermodynamic forcings, Part I: Modeling
 741 strategies and simulations of TOGA COARE convective systems, *J. Atmos. Sci.*,
 742 59, 3492–3518.
- 743 Jung, M., M. Reichstein, and A. Bondeau (2009), Towards global empirical upscaling
 744 of FLUXNET eddy covariance observations: Validation of a model tree ensemble
 745 approach using a biosphere model, *Biogeosciences*, 6, 2001-2013.
- 746 Khairoutdinov, M. F., and D. A. Randall (2001), A cloud resolving model as a cloud
 747 parameterization in the NCAR Community Climate System Model: Preliminary
 748 results, *Geophys. Res. Lett.*, 28, 3617–3620.
- 749 Khairoutdinov, M. F., and D. A. Randall (2003), Cloud resolving modeling of the ARM
 750 summer 1997 IOP: Model formulation, results, uncertainties, and sensitivities, *J.*
 751 *Atmos. Sci.*, 60, 607–625, doi:10.1175/1520-
 752 0469(2003)060<0607:CRMOTA>2.0.CO;2.
- 753 Khairoutdinov, M., D. Randall, and C. DeMott (2005), Simulations of the atmospheric
 754 general circulation using a cloud-resolving model as a superparameterization of
 755 physical processes, *J. Atmos. Sci.*, 62, 2136-2154, doi: 10.1175/JAS3453.1.
- 756 Khairoutdinov, M., C. DeMott, and D. Randall (2008), Evaluation of the simulated
 757 interannual and subseasonal variability in an AMIP-style simulation using the CSU

758 Multiscale Modeling Framework, *J. Clim.*, 21, 413-431,
 759 doi:10.1175/2007JCLI1630.1.

760 Kidd, C., T. Matsui, J.-D. Chern, K. I. Mohr, C. Kummerow, and D. Randel (2016),
 761 Global precipitation estimates from cross-track passive microwave observations
 762 using a physically based retrieval scheme, *J. Hydrometeorol.*, 17, 383-400, doi:
 763 10.1175/JHM-D-15-0051.1.

764 Kim, D., A. H. Sobel, E. D. Maloney, D. M. W. Frierson, and I. S. Kang (2011), A
 765 systematic relationship between intraseasonal variability and mean state bias in
 766 AGCM simulations, *J. Clim.*, 24, 5506-5520, doi:10.1175/2011JCLI4177.1.

767 Kodama, C., et al. (2015), A 20-Year climatology of a NICAM AMIP-type simulation,
 768 *J. Meteorol. Soc. Jpn.*, 93, 393-424, doi:10.2151/jmsj.2015-024.

769 Kooperman, G. J., M. S. Pritchard, S. J. Ghan, M. Wang, R. C. J. Somerville, and L.
 770 M. Russell (2012), Constraining the influence of natural variability to improve
 771 estimates of global aerosol indirect effects in a nudged version of the Community
 772 Atmosphere Model 5, *J. Geophys. Res.-Atmos.*, 117, doi:10.1029/2012JD018588.

773 Lang, S., W.-K. Tao, J. Simpson, and B. Ferrier (2003), Modeling of convective-
 774 stratiform precipitation processes: Sensitivity to partitioning methods, *J. Appl.*
 775 *Meteorol.*, 42, 505-527, doi:10.1175/1520-
 776 0450(2003)042<0505:MOCSP>2.0.CO;2.

777 Lang, S., W.-K. Tao, J.-D. Chern, D. Wu, and X. Li (2014), Benefits of a 4th ice class
 778 in the simulated radar reflectivities of convective systems using a bulk
 779 microphysics scheme, *J. Atmos. Sci.*, 71, 3583-3612, doi:10.1175/JAS-D-13-
 780 0330.1.

- 781 Legates, D. R., and C. J. Willmott (1990), Mean seasonal and spatial variability in
 782 global surface air temperature, *Theor. Appl. Climatol.*, *41*, 11–21,
 783 doi:10.1007/BF00866198.
- 784 LeMone, M. A., G. M. Barnes, and E. J. Zipser (1984), Momentum flux by lines of
 785 cumulonimbus over the tropical oceans, *J. Atmos. Sci.*, *41*(12), 1914–1932,
 786 doi:10.1175/1520-0469(1984)041<1914:MFBLOC>2.0.CO;2.
- 787 Li, F., D. Rosa, W. D. Collins, and M. F. Wehner (2012), “Super-parameterization”:
 788 A better way to simulate regional extreme precipitation? *J. Adv. Model. Earth Syst.*,
 789 *4*, M04002, doi:10.1029/2011MS000106.
- 790 Luo, Z., and G. L. Stephens (2006), An enhanced convection-wind-evaporation
 791 feedback in a superparameterization GCM (SP-GCM) depiction of the Asian
 792 summer monsoon, *Geophys. Res. Lett.*, *33*, L06707, doi:10.1029/2005GL025060.
- 793 Marchand, R., J. Haynes, G. G. Mace, T. Ackerman, and G. Stephens (2009), A
 794 comparison of simulated cloud radar output from the multiscale modeling
 795 framework global climate model with CloudSat cloud radar observations, *J.*
 796 *Geophys. Res.-Atmos.*, *114*, D00A20, doi:10.1029/2008JD009790.
- 797 Marchand, R., and T. Ackerman (2010), An analysis of cloud cover in multiscale
 798 modeling framework global climate model simulations using 4 and 1 km horizontal
 799 grids, *J. Geophys. Res.*, *115*, D16207, doi:10.1029/2009JD013423.
- 800 Matsui, T., J.-D. Chern, W.-K. Tao, S. Lang, M. Satoh, T. Hashino, and T. Kubota,
 801 (2016), On the land-ocean contrast of tropical convection and microphysics
 802 statistics derived from TRMM satellite signals and global storm-resolving models.
 803 *J. Hydrometeorol.*, *17*, 1425–1445, doi:10.1175/JHM-D-15-0111.1.

- 804 Miyamoto, Y., Y. Kajikawa, R. Yoshida, T. Yamaura, H. Yashiro, and H. Tomita
 805 (2013), Deep moist atmospheric convection in a subkilometer global simulation,
 806 *Geophys. Res. Lett.*, *40*, 4922-4926, doi:10.1002/grl.50944.
- 807 Mohr, K. I., W.-K. Tao, J.-D. Chern, S. V. Kumar, and C. D. Peters-Lidard (2013), The
 808 NASA-Goddard Multi-scale Modeling Framework-Land Information System:
 809 Global land/atmosphere interaction with resolved convection, *Environ. Modell.*
 810 *Softw.*, *39*103-115, doi:10.1016/j.envsoft.2012.02.023.
- 811 Moncrieff, M.W. (2004), Analytic representation of the large-scale organization of
 812 tropical convection, *J. Atmos. Sci.*, *61*, 1521-1538.
- 813 Nesbitt, S. W., R. Cifelli, and S. A. Rutledge (2006), Storm morphology and rainfall
 814 characteristics of TRMM precipitation features, *Mon. Wea. Rev.*, *134*, 2702–2721.
- 815 Ooyama, K. V. (2001), A dynamic and thermodynamic foundation for modeling the
 816 moist atmosphere with parameterized microphysics, *J. Atmos. Sci.*, *58*, 2073–2102,
 817 doi:10.1175/1520-0469(2001)058<2073:ADATFF>2.0.CO;2.
- 818 Ovtchinnikov, M., T. Ackerman, R. Marchand, and M. Khairoutdinov (2006),
 819 Evaluation of the multiscale modeling framework using data from the Atmospheric
 820 Radiation Measurement Program, *J. Clim.*, *19*, 1716-1729.
- 821 Petch, J. C., and M. E. B. Gray (2001), Sensitivity studies using a cloud-resolving
 822 model simulation of the tropical west Pacific, *Q. J. R. Meteorol. Soc.*, *127*, 2287–
 823 2306.
- 824 Pritchard, M. S., and R. C. J. Somerville (2009), Assessing the diurnal cycle of
 825 precipitation in a multi- scale climate model, *J. Adv. Model. Earth Syst.*, *1*,
 826 doi:10.3894/JAMES.2009.1.12

- 827 Pritchard, M. S., M. W. Moncrieff, and R. C. J. Somerville (2011), Orographic
 828 propagating precipitation systems over the United States in a global climate model
 829 with embedded explicit convection, *J. Atmos. Sci.*, *68*, 1821-1840,
 830 doi:10.1175/2011JAS3699.1.
- 831 Pritchard, M. S., and C. S. Bretherton (2014), Causal evidence that rotational moisture
 832 advection is critical to the superparameterized Madden-Julian oscillation, *J. Atmos.*
 833 *Sci.*, *71*, 800-815, doi:10.1175/JAS-D-13-0119.1.
- 834 Pritchard, M. S., C. S. Bretherton, and C. A. DeMott (2014), Restricting 32–128 km
 835 horizontal scales hardly affects the MJO in the Superparameterized Community
 836 Atmosphere Model v.3.0 but the number of cloud-resolving grid columns
 837 constrains vertical mixing, *J. Adv. Model. Earth Syst.*, *6*, 723–739,
 838 doi:10.1002/2014MS000340.
- 839 Putman, W. M., and M. Suarez (2011), Cloud-system resolving simulations with the
 840 NASA Goddard Earth Observing System global atmospheric model (GEOS-5),
 841 *Geophys. Res. Lett.*, *38*, L16809, doi:10.1029/2011GL048438.
- 842 Randall, D. A., M. Khairoutdinov, A. Arakawa, and W. Grabowski (2003), Breaking
 843 the cloud parameterization deadlock, *Bull. Am. Meteorol. Soc.*, *84*, 1547-1564.
- 844 Randall, D., C. DeMott, C. Stan, M. Khairoutdinov, J. Benedict, R. McCrary, K.
 845 Thayer-Calder, and M. Branson (2016), Simulations of the tropical general
 846 circulation with a multiscale global model, *Meteorol. Monogr.*, *56*, 15.1-15.15, doi:
 847 10.1175/AMSMONOGRAPHS-D-15-0016.1.
- 848 Reynolds, R. W., et al. (2007), Daily high-resolution-blended analyses for sea surface
 849 temperature, *J. Clim.*, *20*, 5473-5496, doi:10.1175/2007JCLI1824.1.

- 850 Rosa, D., J. F. Lamarque, and W. D. Collins (2012), Global transport of passive tracers
 851 in conventional and superparameterized climate models: Evaluation of multi-scale
 852 methods, *J. Adv. Model. Earth Syst.*, *4*, M10003, doi:10.1029/2012MS000206.
- 853 Rosa, D., and W. D. Collins (2013), A case study of subdaily simulated and observed
 854 continental convective precipitation: CMIP5 and multiscale global climate models
 855 comparison, *Geophys. Res. Lett.*, *40*, 5999–6003, doi:10.1002/2013GL057987.
- 856 Satoh, M., H. Tomita, H. Miura, S. Iga, and T. Nasuno (2005), Development of a global
 857 cloud resolving model--a multi-scale structure of tropical convections, *J. Earth*
 858 *Simulator*, *3*, 11-19.
- 859 Satoh, M., et al. (2008), Nonhydrostatic Icosahedral Atmospheric Model (NICAM) for
 860 global cloud resolving simulations, *J. Comput. Phys.*, *227*, 3486–3514,
 861 doi:10.1016/j.jcp.2007.02.006.
- 862 Satoh, M., et al. (2014), The Non-hydrostatic Icosahedral Atmospheric Model:
 863 description and development, *Progress in Earth and Planetary Science*, *1*:18,
 864 doi:10.1186/s40645-014-0018-1.
- 865 Schumacher, C., R. A. Houze, and I. Kraucunas (2004), The tropical dynamical
 866 response to latent heating estimates derived from the TRMM precipitation radar, *J.*
 867 *Atmos. Sci.*, *61*, 1341-1358.
- 868 Skamarock, W. C., S.-H. Park, J. B. Klemp, and C. Snyder (2014), Atmospheric kinetic
 869 energy spectra from global high-resolution nonhydrostatic simulations, *J. Atmos.*
 870 *Sci.*, *71*, 4369-4381, doi:10.1175/JAS-D-14-0114.1.
- 871 Simpson, J., C. Kummerow, W.-K. Tao, and R. F. Adler (1996), On the Tropical
 872 Rainfall Measuring Mission (TRMM), *Meteorol. Atmos. Phys.*, *60*, 19-36.

- 873 Soong, S.-T., and W.-K. Tao (1984), A numerical study of the vertical transport of
 874 momentum in a tropical rainband, *J. Atmos. Sci.*, *41*(6), 1049-1061,
 875 doi:10.1175/1520-0469(1984)041<1049:ANSOTV>2.0CO;2.
- 876 Stan, C., M. Khairoutdinov, C. A. DeMott, V. Krishnamurthy, D. M. Straus, D. A.
 877 Randall, J. L. Kinter III, and J. Shukla (2010), An ocean-atmosphere climate
 878 simulation with an embedded cloud resolving model, *Geophys. Res. Lett.*, *37*,
 879 L01702, doi:10.1029/2009GL040822.
- 880 Stan, C., and L. Xu (2014), Climate simulations and projections with a super-
 881 parameterized climate model, *Environ. Modell. Softw.*, *60*, 134-152,
 882 doi:10.1016/j.envsoft.2014.06.013.
- 883 Steiner, M., R. A. Houze Jr., and S. E. Yuter, 1995: Climatological characteristics of
 884 three-dimensional storm structure from operational radar and rain gauge data. *J.*
 885 *Appl. Meteorol.*, *34*, 1978–2007.
- 886 Tao, W.-K., S. E. Lang, J. Simpson, and R. Adler (1993), Retrieval algorithms for
 887 estimating the vertical profiles of latent heat release: Their applications for TRMM,
 888 *J. Meteorol. Soc. Jpn.*, *71*, 685–700.
- 889 Tao, W.-K., et al. (2009), A multiscale modeling system: Developments, applications,
 890 and critical Issues, *Bull. Am. Meteorol. Soc.*, *90*, 515-534,
 891 doi:10.1175/2008BAMS2542.1.
- 892 Tao, W.-K., et al. (2014), The Goddard Cumulus Ensemble model (GCE):
 893 Improvements and applications for studying precipitation processes, *Atmos. Res.*,
 894 *143*, 392-424, doi:10.1016/j.atmosres.2014.03.005.
- 895 Tao, W.-K., D. Wu, S. E. Lang, J.-D. Chern, C. D. Peters-Lidard, A. Fridlind, and T.

- 896 Matsui (2016), High-resolution NU-WRF simulations of a deep convective-
 897 precipitation system during MC3E: Further improvements and comparisons
 898 between Goddard microphysics schemes and observations, *J. Geophys. Res.-*
 899 *Atmos.*, *121*, 1278–1305, doi:10.1002/2015JD023986.
- 900 Thayer-Calder, K., and D. A. Randall (2009), The role of convective moistening in the
 901 Madden-Julian oscillation, *J. Atmos. Sci.*, *66*, 3297-3312,
 902 doi:10.1175/2009JAS3081.1.
- 903 Tomita, H., et al. (2005), A global cloud-resolving simulation: Preliminary results from
 904 an aqua planet experiment, *Geophys. Res. Lett.*, *32*, L08805,
 905 doi:10.1029/2005GL022459.
- 906 Tulich, S. N. (2015), A strategy for representing the effects of convective momentum
 907 transport in multiscale models: Evaluation using a new superparameterized version
 908 of the Weather Research and Forecast model (SP-WRF), *J. Adv. Model. Earth Syst.*,
 909 *7*, 938-062, doi:10.1002/2014MS0004617.
- 910 Tompkins, A. M. (2000), The impact of dimensionality on longterm cloud-resolving
 911 model simulations, *Mon. Wea. Rev.*, *128*, 1521–1535.
- 912 Wang, M., S. Ghan, M. Ovchinnikov, X. Liu, R. Easter, E. Kassianov, Y. Qian, and H.
 913 Morrison (2011), Aerosol indirect effects in a multi-scale aerosol-climate model
 914 PNNL-MMF, *Atmos. Chem. Phys.*, *11*(11), 5431-5455.
- 915 Wang, M., et al. (2012), Constraining cloud lifetime effects of aerosols using A-Train
 916 satellite observations, *Geophys. Res. Lett.*, *39*, L15709, 10.1029/2012GL052204.
- 917 Wang, M., V. E. Larson, S. Ghan, M. Ovchinnikov, D. P. Schanen, H. Xiao, X. Liu,
 918 P. Rasch, and Z. Guo (2015), A multiscale modeling framework model

- 919 (superparameterized CAM5) with a higher-order turbulence closure: Model
 920 description and low-cloud simulations, *J. Adv. Model. Earth Syst.*, 7,
 921 doi:10.1002/2014MS000375.
- 922 Wyant, M. C., M. Khairoutdinov, and C. S. Bretherton (2006), Climate sensitivity and
 923 cloud response of a GCM with a superparameterization, *Geophys. Res. Lett.*, 33,
 924 L06714, doi:10.1029/2005GL025464.
- 925 Wyant, M. C., C. S. Bretherton, and P. N. Blossey (2009), Subtropical low cloud
 926 response to a warmer climate in a superparameterized climate model. Part I:
 927 Regime sorting and physical mechanisms, *J. Adv. Model. Earth Syst.*, 1,
 928 doi:10.3894/JAMES.2009.1.7
- 929 Wyant, M. C., C. S. Bretherton, P. N. Blossey, and M. Khairoutdinov (2012), Fast
 930 cloud adjustment to increasing CO₂ in a superparameterized climate model, *J. Adv.*
 931 *Model. Earth Syst.*, 4, 10.1029/2011MS000092.
- 932 Xu, K. M., and A. Cheng (2013a), Evaluating low cloud simulation from an upgraded
 933 Multiscale Modeling Framework model. Part I: Sensitivity to spatial resolution and
 934 climatology, *J. Clim.*, 26, 5717-5740, doi: 10.1175/JCLI-D-12-00200.1.
- 935 Xu, K.-M., and A. Cheng (2013b), Evaluating low-cloud simulation from an upgraded
 936 Multiscale Modeling Framework model, Part II: Seasonal variations over the
 937 Eastern Pacific, *J. Clim.*, 26, 5741-5760, doi:10.1175/JCLI-D-12-00276.1.
- 938 Yashiro, H., Y. Kajikawa, Y. Miyamoto, T. Yamaura, R. Yoshida, and H. Tomita
 939 (2016), Resolution dependence of the diurnal cycle of precipitation simulated by a
 940 global cloud system resolving model, *SOLA*, 12, 272-276, doi:10.2151/sola.2016-
 941 053.

- 942 Yoneyama, K., C. Zhang, and C. N. Long (2013), Tracking pulses of the Madden-
943 Julian oscillation, *Bull. Am. Meteorol. Soc.*, *94*, 1871-1891, doi: 10.1175/BAMS-
944 D-12-00157.1.
- 945 Yu, L., and R. A. Weller (2007), Objectively analyzed air–sea heat fluxes for the global
946 ice-free oceans (1981–2005), *Bull. Am. Meteorol. Soc.*, *88*, 527–539,
947 doi:10.1175/BAMS-88-4-527.
- 948 Zhang, Y., S. A. Klein, C. Liu, B. Tian, R. T. Marchand, J. M. Haynes, R. B. McCoy,
949 Y. Zhang, and T. P. Ackerman (2008), On the diurnal cycle of deep convection,
950 high-level cloud, and upper troposphere water vapor in the Multiscale Modeling
951 Framework, *J. Geophys. Res.-Atmos.*, *113*, doi:10.1029/2008JD009905.
- 952 Zhu, H., H. Hendon, and C. Jakob (2009), Convection in a parameterized and
953 superparameterized model and its role in the representation of the MJO, *J. Atmos.*
954 *Sci.*, *66*, 2796-2811, doi: 10.1175/2009JAS3097.1
- 955

Reference	GCM resolution	CRM (# of grid/ resolution)	Period of model integration	Total Rainfall (W. Pacific and tropics)
<i>Khairoutdinov et al.</i> [2005]	T42 (~300 km)	64/4 km 8 x 8 /4km	500 days	Overestimated for 2D Better but underestimated for 3D with momentum
<i>Luo and Stephens</i> [2006]	T42 (~300 km)	64/ 4 km	10 months	Overestimated
<i>Ovtchinnikov et al.</i> [2006]	T42 (~300 km)	64/4 km	1999 (SGP/TWP)	Over- and under-estimated
<i>Wyant et al.</i> [2006, 2009]	2.8° x 2.8°	32/4 km	3.67, 5.25 year (+2K SST)	N.A.
<i>DeMott et al.</i> [2007, 2010]	T42 (~300 km)	64/4 km	500 days 1986-1999	Overestimated
<i>Zhang et al.</i> [2008]	2.0° x 2.5°	64/4 km	1998-2002	Overestimated
<i>Khairoutdinov et al.</i> [2008] <i>Kim et al.</i> [2011]	T42 (~300 km)	32/4 km	1985-2004	Overestimated
<i>Benedict and Randall</i> [2009]	2.5° x 2.5°	32/4 km	1985-2004	Overestimated
<i>Theyer-Calder and Randall</i> [2009]	2.0° x 2.5°	64/4 km	1998-2002	Overestimated
<i>Marchand and Ackerman</i> [2009]	2.0° x 2.5°	64/4 km	1997-2002	Overestimated
<i>Pritchard and Somerville</i> [2009]	T42 (~300 km)	32/4 km	2000-2006	Overestimated
<i>Zhu et al.</i> [2009]	T42 (~300 km)	32/4 km	1998-2002	Overestimated
<i>Marchand and Ackerman</i> [2010]	2.0° x 2.5°	64/4 km and 64/1 km	1 year and 1 month	N.A.
<i>Stan et al.</i> [2010]	T42 (~300 km)	32/ 4km	22 years	Overestimated
<i>Stan et al.</i> [2010]* <i>Dirmeyer et al.</i> [2012]	T42 (~300 km) (CCSM)	32/4 km	1979-2006 1998-2009	Overestimated
<i>Benedict and Randall</i> [2011]	2.8° x 2.8° 1D Slab Ocean	32/4 km	1999-2004	Overestimated
<i>Cheng and Xu</i> [2011]	T21 (~400 km)	32/4 km	1990-1992	Underestimated (Compared to Legates and Willmott, 1990)
<i>DeMott et al.</i> [2011]	T42 (~300 km) (CCSM&CAM)	32/4 km	1986-2003	Overestimated (Summer) (Less in CCSM)
<i>Pritchard et al.</i> [2011]	1.9° x 2.5°	64/1km	3 months	Overestimated (USA)
<i>Wang et al.</i> [2011, 2012, 2015]	1.9° x 2.5°	32/4 km	32, 52 months	Overestimated (no aerosol)
<i>Goswami et al.</i> [2011, 2013]	T42 (~300 km)	32/4 km	1997-2008	Overestimated
<i>Rosa et al.</i> [2012] <i>Rosa and Collins</i> [2013]	1.9° x 2.5° 2.0° x 2.5°	64/2 km	1996-2006 1996-2001	Overestimated
<i>Li et al.</i> [2012]	1.875° x 2.0°	64/ 2 km	1996-2001	Overestimated (USA)

<i>Wyant et al.</i> [2012]	2.8° x 2.8°	32/4 km N/S	Climate (4 x CO ₂)	N.A.
<i>Kooperman et al.</i> [2012]	1.9° x 2.5° with nudging and aerosol	32/4 km	1 year	Overestimated
<i>DeMott et al.</i> [2013]	T42 (~300 km) (CCSM)	32/4 km	1998-2010	Overestimated
<i>Xu and Cheng</i> [2013a,b]	1.9° x 2.5°	32/4 km	Last 9 year of 10 year integration	Overestimated
<i>Cheng and Xu</i> [2014]	T21 (~400km)	32/4 km	1990-1992	See Text
<i>Pritchard and Bretherton</i> [2014]	T42 (~300 km)	32/4 km	1980-1986	N.A.
<i>Stan and Xu</i> [2014]	1.9° x 2.5° 0.9° x 1.25°	32/4 km 32/3 km	1979-2010	Overestimated
<i>Pritchard et al.</i> [2014]	T42 (~300 km)	32/4 km 16/4km 8/4km	1980-1990	Overestimated
<i>Tao et al.</i> [2009]	2.5° x 2.0°	32/4 km	1998 - 1999	Overestimated
<i>Tao et al.</i> [2014]	2.5° x 2°	32/4 km	1998 - 2013	Overestimated
<i>Mohr et al.</i> [2013]	2.5° x 2°	32/4 km	2007-2008	Overestimated
<i>Kidd et al.</i> [2016]	2.5° x 2.0°	64/4 km	2007 (nudged to ERA-Interim)	Underestimated
<i>Chern et al.</i> [2016]	2.5° x 2.0°	32/4 km	2007-2008	Overestimated
<i>Matsui et al.</i> [2016]	2.5° x 2.0°	64/4 km	June 2008	Overestimated
<i>Tao and Chern</i> [2016] the present paper	2.5° x 2.0°	32/4 km 64 /4 km 128/2 km 256/1 km	2007-2008	Overestimated

Table 1 Key MMF papers and their model configuration in terms of GCM resolution and number of embedded CRM grid columns and their resolution. The period of model integration and the precipitation bias are also shown.

* See *Dirmeyer et al.* [2012]

964

	CRM grid columns	CRM grid spacing	CRM domain size	GEOS grid spacing	Time Integration
M32	32	4 km	128 km	2°x2.5°	2 years
M64	64	4 km	256 km	2°x2.5°	2 years
M128	128	2 km	256 km	2°x2.5°	2 years
M256	256	1 km	256 km	2°x2.5°	2 years
C32	32	4 km	128 km	No	10 days
C64	64	4 km	256 km	No	10 days
C128	128	2 km	256 km	No	10 days
C256	256	1 km	256 km	No	10 days

965

966

967

968

969

Table 2 Experiment name and model configuration for 4 GMMF (M32, M64, M128 and M256) and 4 GCE simulations (C32, C64, C128, and C256). The GEOS grid spacing is 2.5° and 2.0° in longitude and latitude, respectively.

970

	C32	C64	C128	C256
Convective (mm day ⁻¹)	5.52	5.63	6.35	6.25
Stratiform (mm day ⁻¹)	7.34	7.67	7.04	7.01
Stratiform (%)	57	57	53	53
Total Rainfall (mm day ⁻¹)	12.86	13.37	13.39	13.26
Correlation	0.73	0.79	0.84	0.90
Bias (mm day ⁻¹)	-0.17	0.33	0.36	0.23

971

972 Table 3 Convective, stratiform, and total rainfall (in mm day⁻¹), the stratiform fraction
 973 (%), temporal correlation and domain mean rainfall bias for the C32, C64,
 974 C128 and C256 experiments.

975

976

	M32	M64	M128	M256
Global total Precipitation (mm day ⁻¹) (90°S-90°N)	2.93	2.89	2.86	2.83
Tropical rainfall (mm day ⁻¹) (38°S-38°N)	3.27	3.20	3.17	3.12
Tropical convective rainfall (mm day ⁻¹) (38°S-38°N)	1.466	1.568	1.324	1.169
Tropical stratiform rainfall (mm day ⁻¹) (38°S-38°N)	1.804	1.637	1.849	1.956
Tropical stratiform percentage (%) (38°S-38°N)	55	51	58	63
Correlation (GMMF and GPCP)	0.817	0.814	0.839	0.842
Correlation (GMMF and TRMM 3A25)	0.825	0.825	0.851	0.857
Bias (vs GPCP)	0.27	0.23	0.20	0.17
Bias (vs TRMM 3A25)	0.36	0.30	0.26	0.22
RMSE (vs GPCP)	1.74	1.66	1.47	1.37
RMSE (vs TRMM 3A25)	1.85	1.75	1.54	1.42

Table 4 Total global precipitation, tropical rainfall and its convective and stratiform components (in mm day⁻¹) and stratiform percentage from the M32, M64, M128 and M256 experiments. Two sets of spatial correlation, bias, and root-mean-square error (RMSE) are computed between the GMMF simulations and TRMM 3A25 (38°S - 38°N) and GMMF simulations and GPCP (90°S - 90°N) products, respectively.

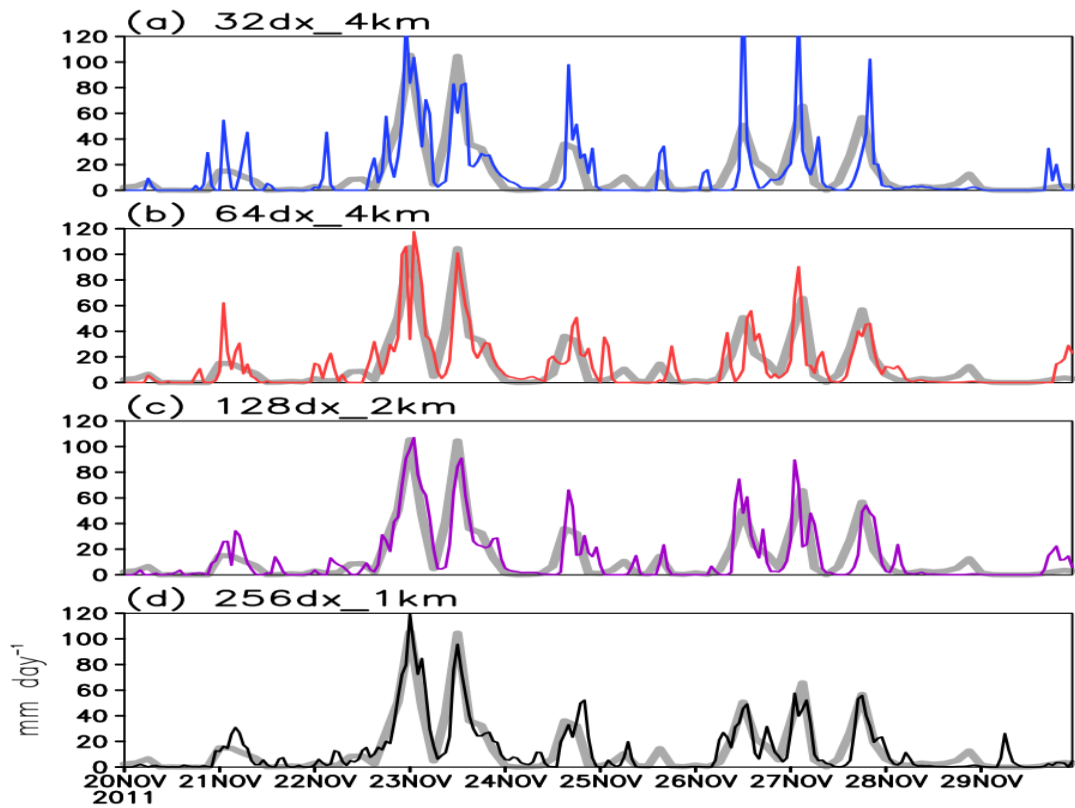
986

	observations	M32	M64	M128	M256
Global total precipitation rate (mm day ⁻¹)	2.659	2.931	2.885	2.860	2.830
Global total precipitation rate (mm day ⁻¹) from ocean	2.001	2.424	2.359	2.326	2.293
Global total precipitation rate (mm day ⁻¹) from land	0.662	0.507	0.526	0.534	0.537
Precipitation rate (mm day ⁻¹) over tropical ocean (15°S-15°N)	3.769	5.782	5.611	5.380	5.248
Global total sfc evaporation rate (mm day ⁻¹)	2.708	2.979	2.923	2.892	2.858
Global total sfc evaporation rate (mm day ⁻¹) from ocean	2.350	2.702	2.633	2.598	2.556
Global total sfc evaporation rate (mm day ⁻¹) from land	0.382	0.277	0.290	0.294	0.302
Sfc evaporation rate (mm day ⁻¹) over tropical ocean (15°S -15°N)	3.592	5.255	4.931	4.815	4.686

987

988 Table 5 GMMF-simulated global and regional mean surface precipitation and
 989 evaporation rates (mm day⁻¹). Observed precipitation and evaporation rates
 990 over ocean and the evaporation rate over land come from GPCP, OAFlux,
 991 and FLUXNET, respectively. For surface evaporation, the same OAFlux
 992 observation points over ocean and FLUXNET points over land are used in
 993 the GMMF calculations (i.e., observed missing points are omitted in the
 994 GMMF).
 995

996



997

998

999

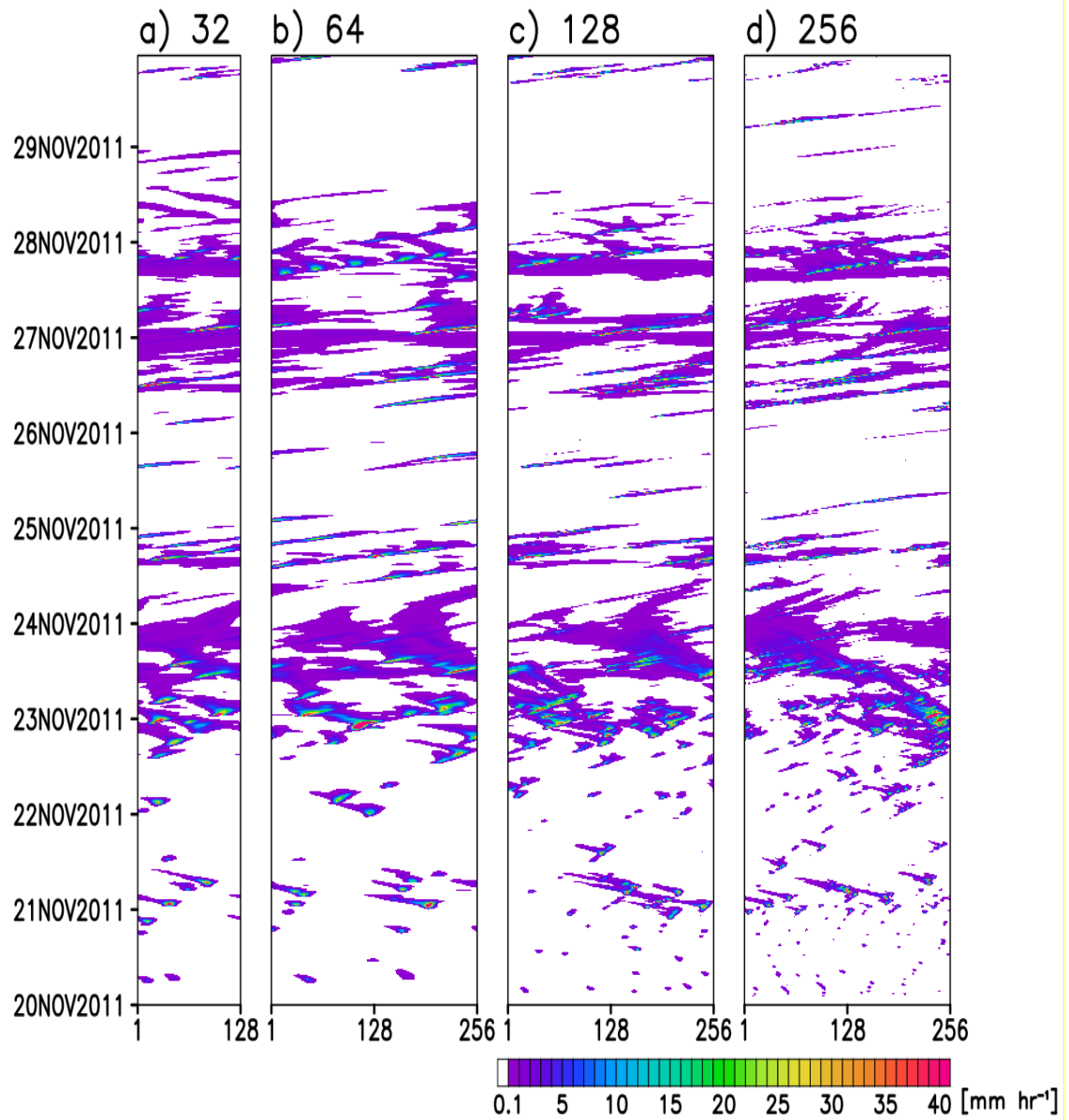
1000

1001

1002

Fig. 1 Time series of GCE domain mean surface rainfall (mm day⁻¹) for the a) C32, b) C64, c) C128 and d) C256 experiments. Thick solid lines show the observed domain mean surface rainfall from the DYNAMO field campaign.

1003



1004
 1005
 1006
 1007
 1008

Fig. 2 Hovmoller diagrams of GCE model-simulated surface rainfall rate (mm h⁻¹) for the a) C32, b) C64, c) C128 and d) C256 experiments.

1009

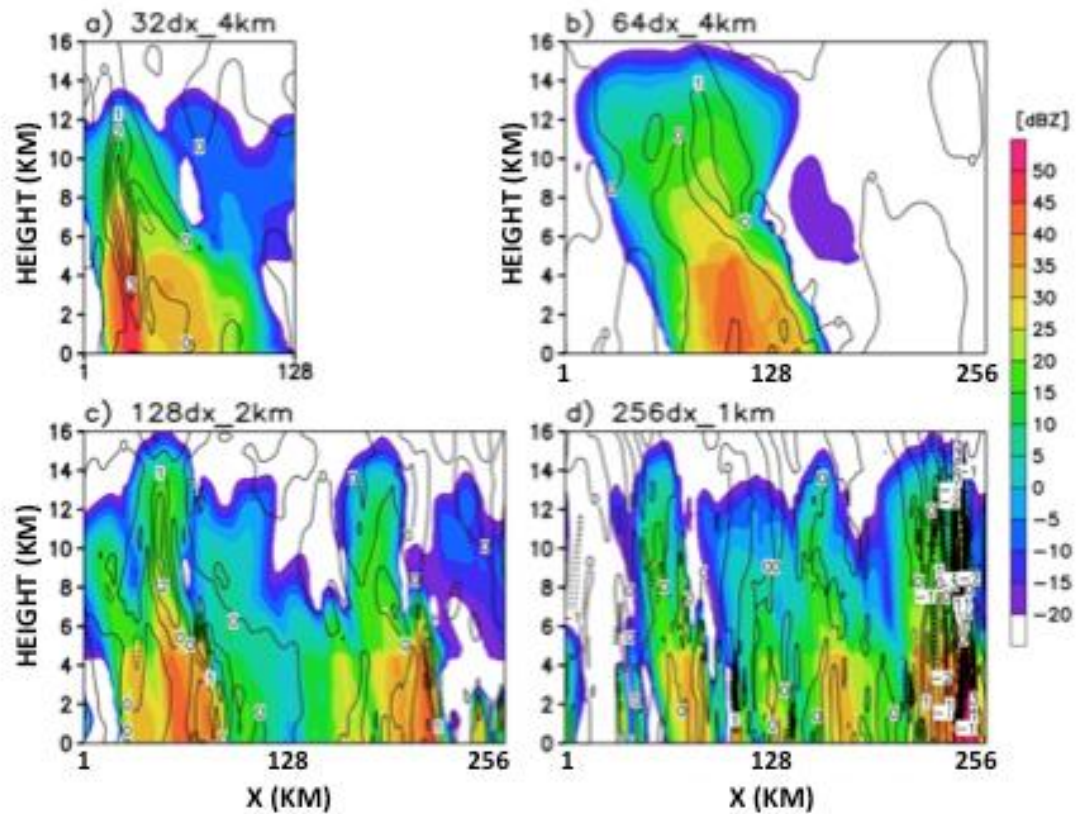


Fig. 3 CRM-simulated radar reflectivity (dBZ, color shading) and vertical velocity (m s⁻¹, contours) at 23 UTC 22 November 2011 (near the time of the peak observed rainfall) for the sensitivity runs a) C32, b) C64, c) C128, and d) C256.

1010
1011
1012
1013
1014
1015
1016

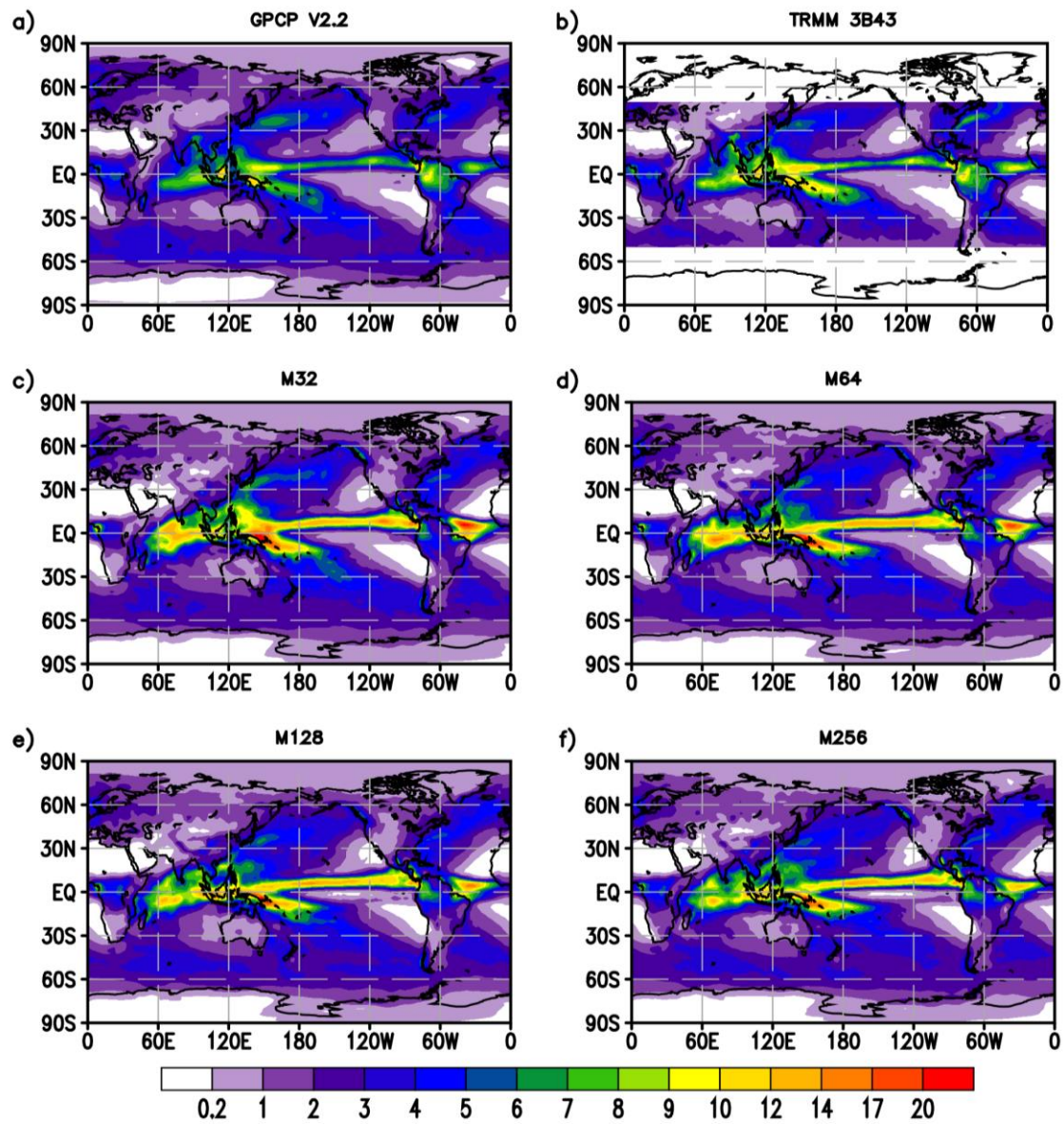
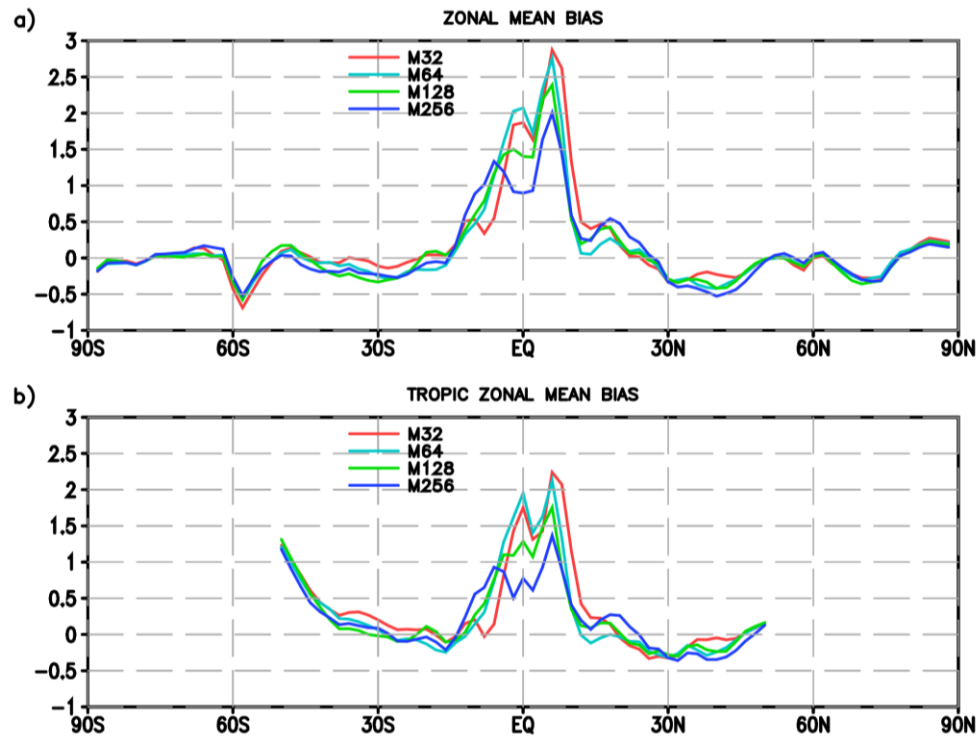


Fig. 4 Two-year (2007-2008) mean precipitation rates (mm day^{-1}) from a) GPCP and b) TRMM 3B43 observations and GMMF simulations for the c) M32, d) M64, e) M128, and f) M256 experiments.

1024



1025

1026

1027 Fig. 5 GMMF mean zonal precipitation rate biases (mm day^{-1}) relative to a) GPCP
 1028 and b) TRMM 3B43 observations. Red, light-blue, green and dark-blue lines
 1029 denote the M32, M64, M128, and M256 experiments, respectively.

1030

Radar reflectivity and W (m/s) at max. precip. time at (76E,2N) in DEC 2007

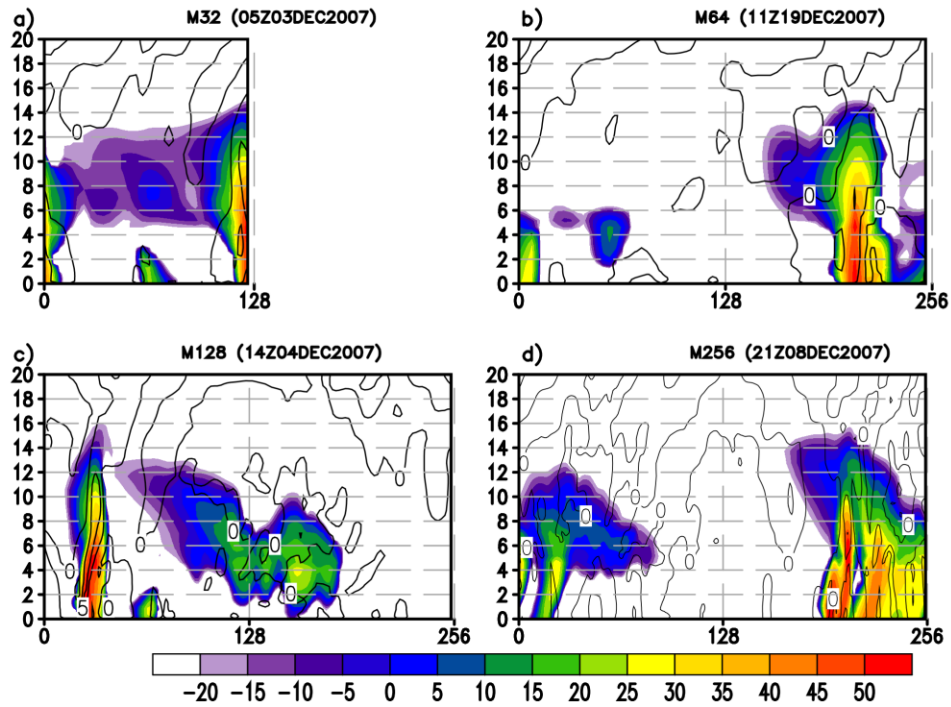


Figure 6 GMMF-simulated radar reflectivity (dBZ, color shading) and vertical velocity (m s^{-1} , contours) at the maximum precipitation time for a GCM grid point at (76°E, 2°N), which is near the DYNAMO field campaign site (76°E, 2°N), in December 2007 for the a) M32, b) M64, c) M128, and d) M256 experiments. The MCSs/squall lines propagate westward except for the M32 case.

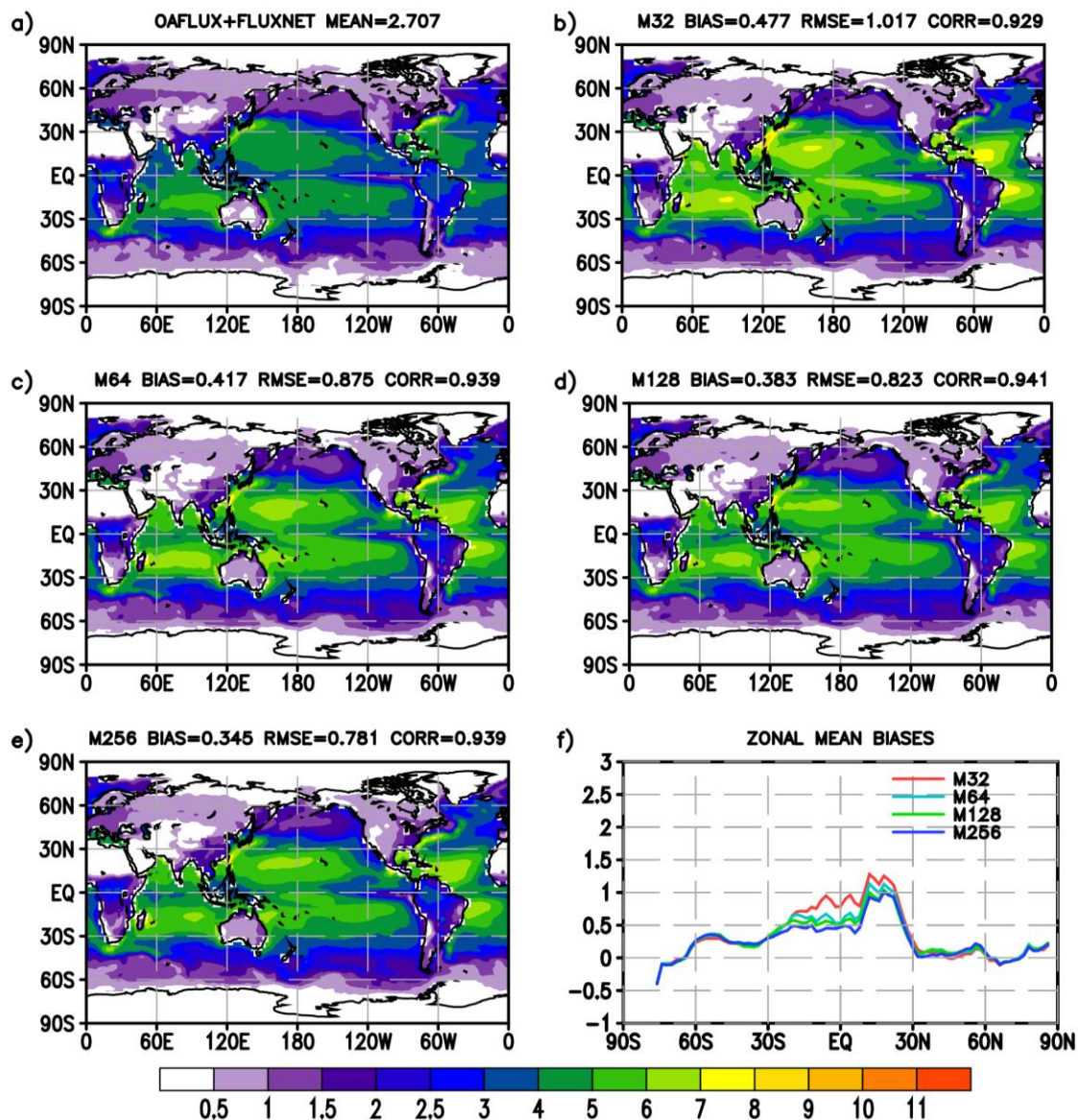


Figure 7 Two-year (2007-2008) mean surface evaporation rate (mm day⁻¹) from a) the combination of OaFlux (over ocean) and FLUXNET (over land) observations and the b) M32, c) M64, d) M128, e) M256 simulations. The GMMF zonal mean biases are given in f) with red, light-blue, green, and dark-blue lines for the M32, M64, M128, and M256 experiments, respectively.

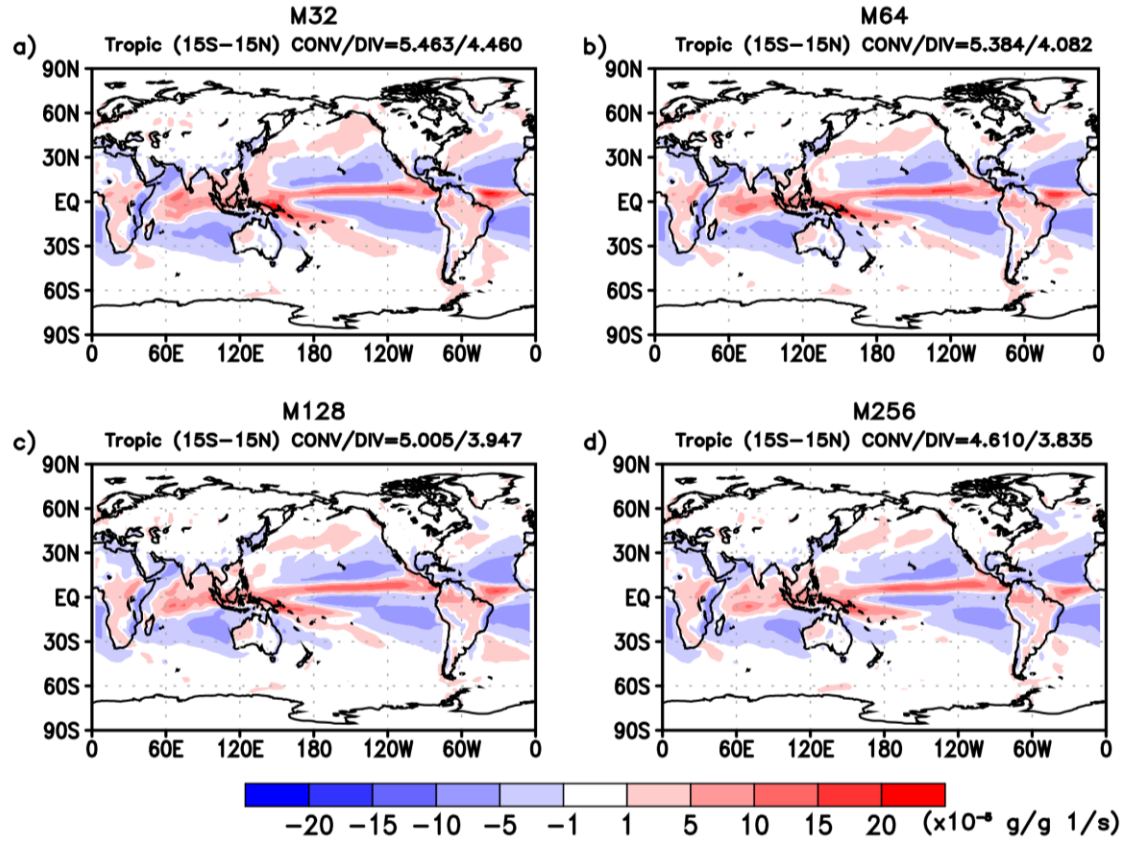


Figure 8 Annual mean low-level (i.e., surface to 700 hPa) moisture flux convergence ($\times 10^{-5} \text{ g g}^{-1} \text{ s}^{-1}$) from the a) M32, b) M64, c) M128, and d) M256 GMMF experiments. The mean moisture flux convergence/divergence amplitude over the Tropics (15°S - 15°N) is also given at the top of each plot.

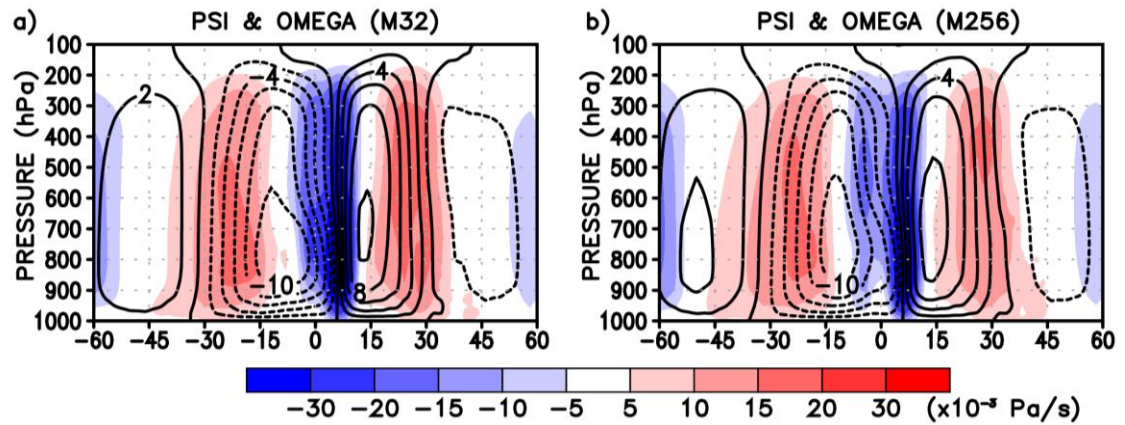


Figure 9 Annual average zonal mean meridional mass stream function values (contours) overlapped with mean vertical pressure velocity (color shading) from the a) M32 and b) M256 GMMF simulations. Units for mass stream function and vertical pressure velocity are $10^{10} \text{ kg s}^{-1}$ and $1.0^{-3} \text{ Pa s}^{-1}$, respectively. Positive (solid contours) and negative (dashed contour) stream function values represent counterclockwise and clockwise circulations, respectively.

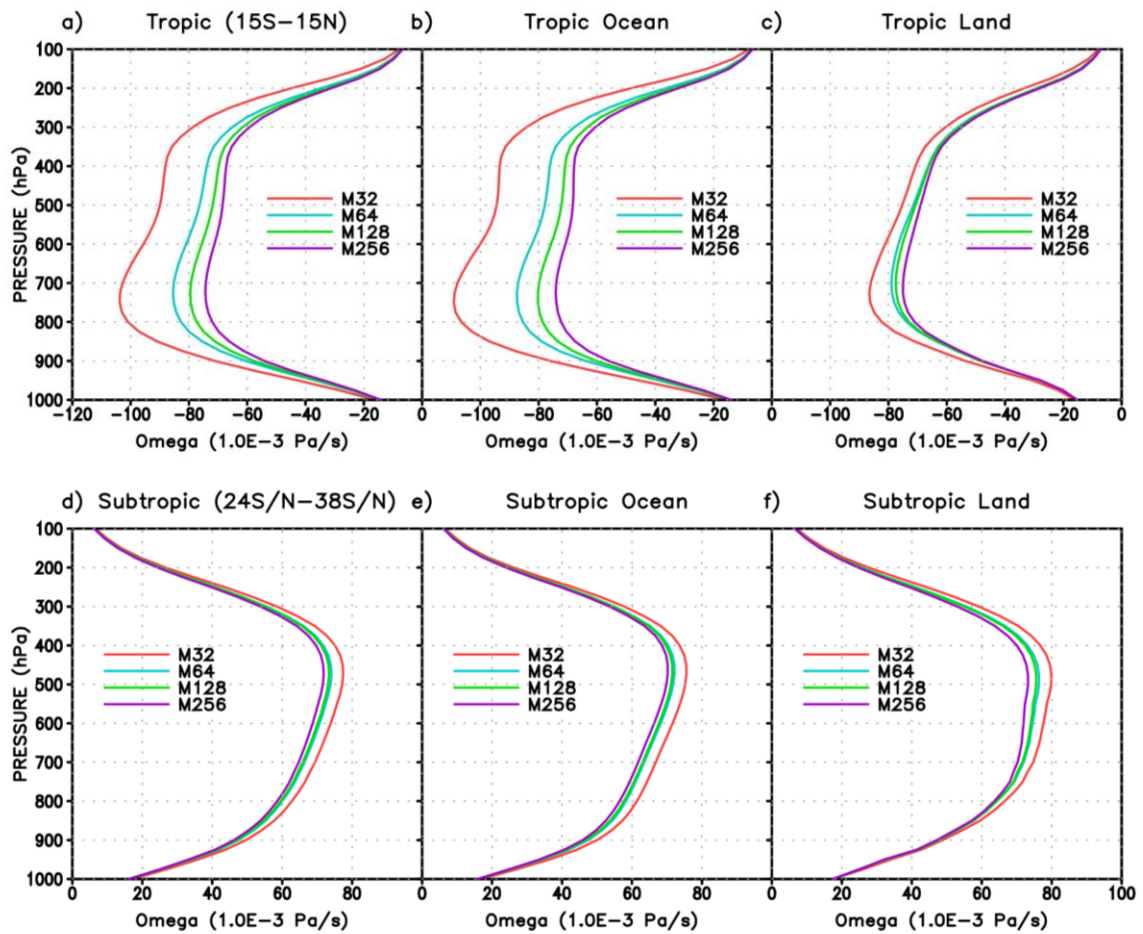
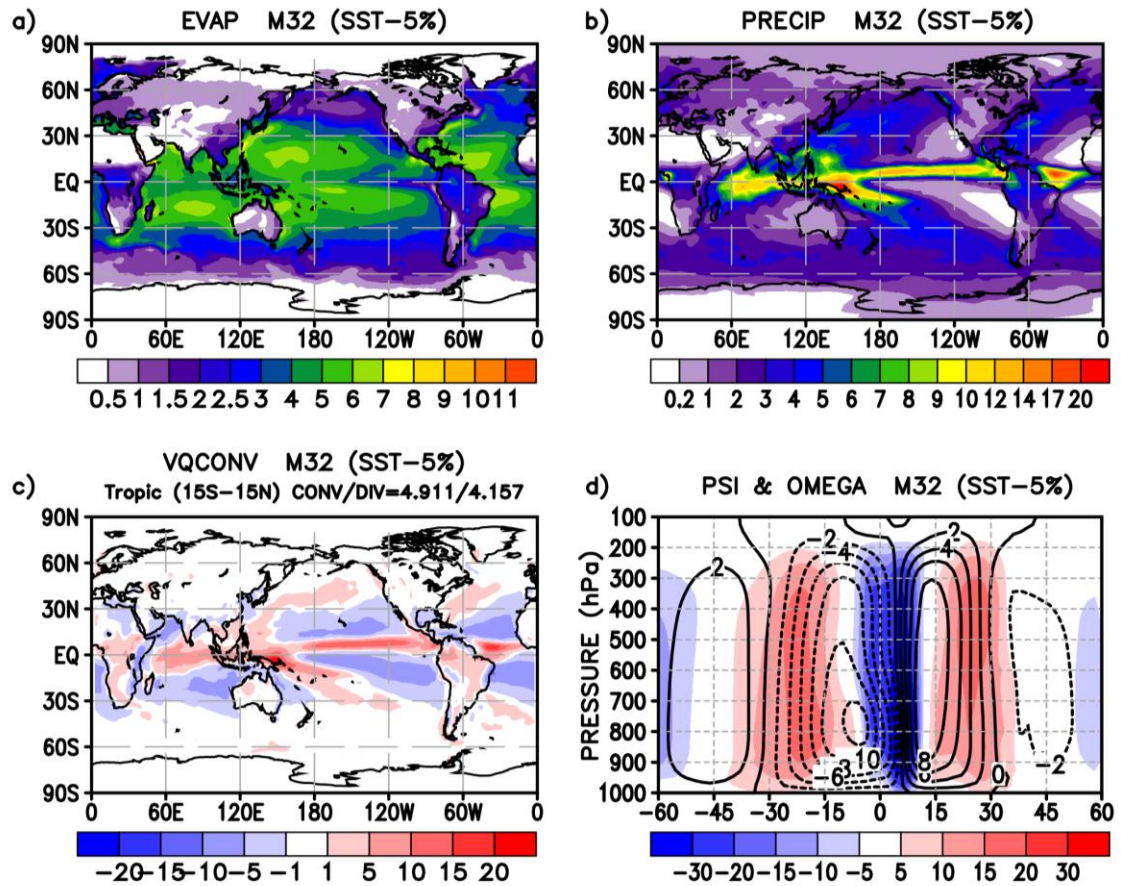


Figure 10 Two-year (2007-2008) mean vertical pressure velocity (1.0^{-3} Pa s^{-1}) for GCM model cells with updrafts from the M32, M64, M128, and M256 GMMF simulations over a) the Tropics (15°S - 15°N), b) tropical ocean, c) tropical land and for GCM model cells with downdrafts over d) the subtropics (24°S/N - 38°S/N), e) subtropical ocean, and f) subtropical land.

1079



1080

1081

1082 Figure 11 Two-year (2007-2008) annual mean a) evaporation rate (mm day⁻¹), b)
 1083 precipitation rate (mm day⁻¹), c) low-level moisture flux convergence (x
 1084 10⁻⁵ g g⁻¹ s⁻¹), and d) zonal mean meridional mass stream function values
 1085 (contours) overlapped with mean vertical pressure velocity (color shading)
 1086 from the GMMF sensitivity experiment with SSTs (in °C) reduced by 5%.
 1087 Units for mass stream function and vertical pressure velocity are 10¹⁰ kg s⁻¹
 1088 and 1.0⁻³ Pa s⁻¹, respectively.
 1089